2023-12-15

Tipping the Mesoscales: Advances in Multipeak Bragg Coherent Diffraction Imaging

J. Nicholas Porter
Brigham Young University

Tipping the Mesoscales: Advances in Multipeak Bragg Coherent Diffraction Imaging

J. Nicholas Porter

A thesis submitted to the faculty of
Brigham Young University
in partial fulfillment of the requirements for the degree of

Master of Science

Richard Sandberg, Chair
David Allred
Brandon Campbell

Department of Physics and Astronomy

Brigham Young University

ABSTRACT

Tipping the Mesoscales: Advances in Multipeak Bragg
Coherent Diffraction Imaging

J. Nicholas Porter
Department of Physics and Astronomy, BYU
Master of Science

Material failure begins with strain between atoms and cascades upward into macroscopic damage such as cracks. Therefore, our ability to predict (and therefore prevent) material failure is largely limited by our understanding of this process. This understanding, however, has been impeded by the difficulty of directly observing such phenomena. In this thesis, I discuss recent advances in Bragg coherent diffraction imaging (BCDI) which produce three-dimensional, mesoscopic images of interior strain in microcrystals. In particular, I present a novel algorithm, based on the concept of cyclic-constrained optimization (CCO), for the rapid, coupled reconstruction of a microcrystal from multiple Bragg diffraction patterns. Using coherent diffraction data collected from the Advanced Photon Source (APS), this algorithm achieves resolution comparable to other multipeak BCDI methods at a fraction of the computational cost. As the rate of data production at coherent X-ray sources worldwide continues to increase, such rapid algorithms will be critical to preventing a data analysis bottleneck. I also present a technique for mapping the orientations of crystal grains on a sample by analyzing the positions of Laue diffraction spots when the crystal is illuminated by a polychromatic beam. Each of these two methods constitute a significant contribution to the field of mesoscopic strain analysis.

Keywords: Bragg coherent diffraction imaging, materials science, computational imaging, high-dimensional optimization, physics education

ACKNOWLEDGMENTS

To Richard Sandberg, thank you for your wisdom, support, kindness, trust, and patience. To Margaret Ludlow and Shelena Shamo, thank you for everything you've done and continue to do behind the scenes so that I could focus on school and research. To my collaborators near and far, David Allred, Taylor Buckway, Branton Campbell, Wonsuk Cha, Julio Escobedo, Barbara Frosik, Yuan Gao, Ross Harder, Andres Herrera, Daniel Hodge, Stephen Hruszkewycz, Nash Karrington, Jason Meziere, Josh Miller, Nathan Powers, Tony Rollett, Landon Schnebly, Bob Suter, Matt Wilkin, Garth Williams, Yueheng Zhang, and anyone I've forgotten, I truly could not have done any of this without you. To my high-school physics teacher Mr. Pagett, thank you for giving me the bug that got me here. To my parents David and Nola Porter, thank you for never giving up on me. Finally, to my children Henry and Grace, and most of all to my angel wife Jenicca, my love and gratitude goes beyond words (and good thing too, since two of you can't read yet).

Contents

List of Figures

List of Tables

Chapter 1

Introduction

1.1 Understanding strain

The modern human is increasingly dependent on materials that can effectively deal with strain. Such materials allow us to build taller buildings, smaller circuits, safer transportation, and cleaner energy grids. However, knowing which material to use for a given application requires (among other things) a detailed, multiscale understanding of the nature and dynamics of strain [1].

For every atom in a crystal lattice, we can define a vector $\mathbf{u}$ as the atom's displacement from the ideal lattice. Because of the nature of a lattice, each atom's displacement vector is typically correlated with its immediate neighbors, such that significant changes typically occur only over the scale of many atoms. Thus, it is often more useful to consider the continuous vector field $\mathbf{u}(\mathbf{r})$, defined as the average atomic displacement at any point. We can then characterize the elastic strain as a tensor [2]:

$$\varepsilon = \frac{1}{2}\left[J\mathbf{u} + (J\mathbf{u})^T\right] = \begin{bmatrix} \frac{\partial \mathbf{u}}{\partial x} & \frac{1}{2}\left(\frac{\partial \mathbf{u}}{\partial x} + \frac{\partial \mathbf{u}}{\partial y}\right) & \frac{1}{2}\left(\frac{\partial \mathbf{u}}{\partial x} + \frac{\partial \mathbf{u}}{\partial z}\right) \\ \frac{1}{2}\left(\frac{\partial \mathbf{u}}{\partial y} + \frac{\partial \mathbf{u}}{\partial x}\right) & \frac{\partial \mathbf{u}}{\partial y} & \frac{1}{2}\left(\frac{\partial \mathbf{u}}{\partial y} + \frac{\partial \mathbf{u}}{\partial z}\right) \\ \frac{1}{2}\left(\frac{\partial \mathbf{u}}{\partial z} + \frac{\partial \mathbf{u}}{\partial x}\right) & \frac{1}{2}\left(\frac{\partial \mathbf{u}}{\partial z} + \frac{\partial \mathbf{u}}{\partial y}\right) & \frac{\partial \mathbf{u}}{\partial z} \end{bmatrix}, \tag{1.1}$$

where J is the Jacobian operator. Due to the redundancy of the diagonal terms, ε is often referred to as the six-component strain tensor, with ε_{xx}, ε_{yy}, and ε_{zz} as its linear components and ε_{xy}, ε_{yz}, and ε_{zx} as its shear components.

Rather than being evenly distributed, strain is often concentrated into crystalline defects, known as dislocations [3]. As stress is applied to the material, the number and positions of these dislocations change in order to minimize potential energy. The motion of a dislocation shows a strong preference for the direction of the Burgers vector. Sources and sinks of dislocations typically occur in regions of high deformation, such as a grain boundary—an interface between differently oriented lattices. Most metals are naturally polycrystalline, i.e. composed of many randomly oriented crystal grains. Many useful properties such as hardenability, malleability, and ductility stem from the distribution and interactions of dislocations and grain boundaries [4, 5]. Therefore, a primary goal of this research is the direct, dynamic observation of a dislocation as it moves to (and possibly through) a grain boundary. This is difficult for two reasons.

The first obstacle to imaging strain in materials is the scale on which such interactions take place. Optical microscopy is limited by the fact that features smaller than ~ 0.5 μm are irresolvable in the visible spectrum [6]. Electron microscopy can image surfaces at much higher spatial resolution, but with a significant tradeoff in temporal resolution. Molecular dynamics (MD) simulations, which model the interactions between atoms over time, have contributed greatly to our understanding of phenomena on the atomic scale (0.1–100 nm). However, the computational cost of such simulations makes them prohibitively expensive to model large numbers of atoms on time scales of seconds. It should be noted that electron microscopy and molecular dynamics are constantly improving their scope. A recent publication describes a scanning transmission electron microscope capturing 92 fps at 128×128 pixel resolution and 5.8 fps at 512×512 [7]. Another highlights a MD program which was able to calculate the motions of just over a billion atoms at a rate of one simulated nanosecond per day by running in parallel on 130,000 linked processor cores [8]. However, these methods still

Figure 1.1 While Superman's "X-ray vision" remains science fiction, it is inspired by fact. Because X rays experience very low absorption when passing through most materials, they have been used for well over a century to see into and through objects that are opaque in the visible spectrum. Image credit: www.greatkrypton.com

struggle to capture the elusive "mesoscale" [9], a world too small and/or fast to see but too large and/or slow to model.

The second obstacle to imaging strain in materials is the fact that these interactions take place inside the (often opaque) materials themselves. While looking at surface behavior has led to many insights [4], strain is an inherently three-dimensional phenomenon, and must be observed as such. Perhaps inspired by the work of Röntgen [10], Superman, or both, some scientists turned to X rays. These high-energy photons interact weakly with matter, mostly passing through it. Furthermore, X rays also circumvent the scale obstacle; they can be measured by fast digital image detectors, and their short (~ 0.1 nm) wavelength provides excellent spatial resolution.

1.2 Bragg coherent diffraction imaging

Bragg coherent diffraction imaging (BCDI) [11–15] is a subset of coherent diffraction imaging (CDI), an umbrella term referring to a number of similar lensless imaging techniques [16]. All forms of CDI involve (1) illuminating a sample with coherent light to create a diffraction pattern,

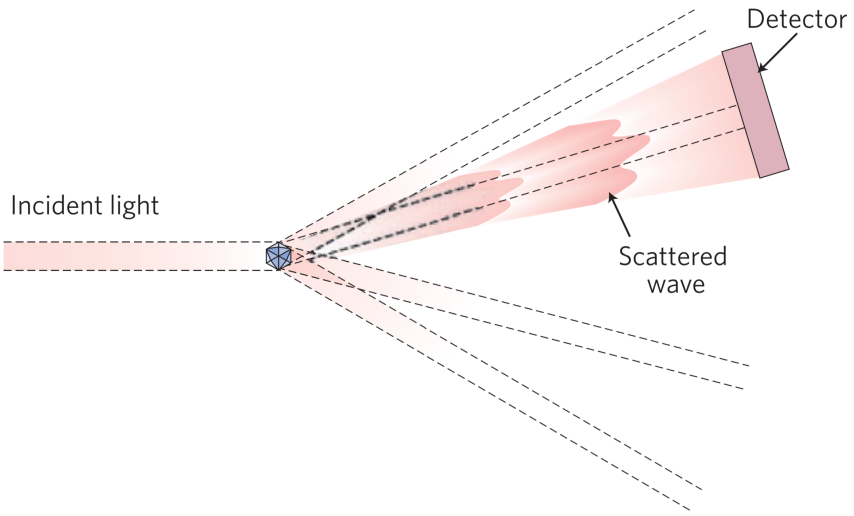

Figure 1.2 A diagram depicting the basic experimental configuration for BCDI. Incident light reflects off a crystal according to the Bragg condition. The resulting diffraction pattern can then be measured and analyzed to gain insight into the crystal's shape and structure. Figure taken from [16].

(2) digitally measuring the intensity profile of the diffraction pattern with an image sensor, and (3) reconstructing an image of the diffracting object by applying specialized algorithms to the measured diffraction pattern [17]. In this section, I will describe these three steps and discuss how the nuances of BCDI make it particularly well suited to probe 3D strain at the mesoscale.

In BCDI, a small crystalline sample is illuminated by a coherent X-ray beam, as shown in Fig. 1.2. Bragg's law states that X rays will reflect off of the atomic planes in a crystal when the Bragg condition ($n\lambda = 2a\sin\theta$) is met [18]. The satisfaction of this condition corresponds to a reciprocal lattice vector that falls on the Ewald sphere [19]. A perfect, infinite crystal—for which the shape function $\rho(\mathbf{r})$ is unity and the atomic displacement field $\mathbf{u}(\mathbf{r})$ is zero—is an array of Dirac delta functions in both real and reciprocal space. In general, however, the crystal's representation in reciprocal space can be written as a convolution,

$$\int_{-\infty}^{\infty} L(\mathbf{r})\rho(\mathbf{r})e^{i\mathbf{q}\cdot\mathbf{u}(\mathbf{r})}e^{i\mathbf{q}\cdot\mathbf{r}}\,d\mathbf{r} \;=\; \hat{L}(\mathbf{q})\otimes\mathscr{F}\left[\rho(\mathbf{r})e^{i\mathbf{q}\cdot\mathbf{u}(\mathbf{r})}\right], \tag{1.2}$$

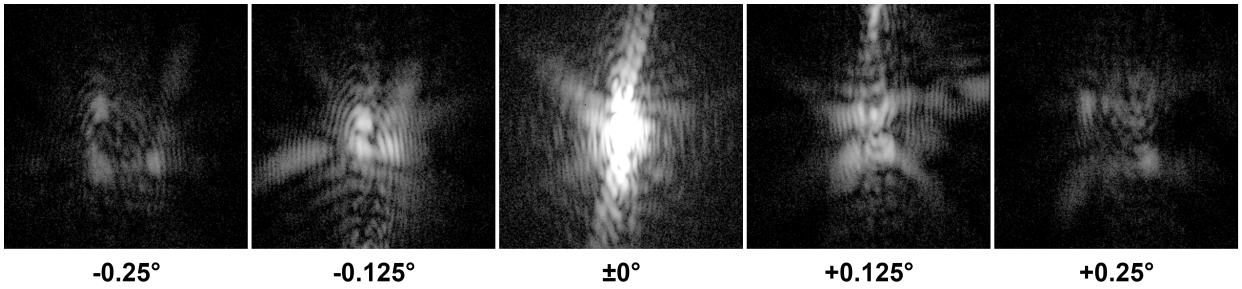

Figure 1.3 A Bragg diffraction pattern sampled at five different θ rotation points near the Bragg condition. When stacked together, these create a 3D image with coordinates (x, y, θ). Note that the highest intensity occurs near the center in all three dimensions.

where $L(\mathbf{r})$ and $\hat{L}(\mathbf{q})$ are respectively the atomic and reciprocal lattice functions, and $\mathscr{F}$ is the Fourier transform [11, 12, 20]. Thus the entire three-dimensional shape and the projection of the displacement field onto the scattering vector are both encoded into the volume around each reciprocal lattice peak.

By "rocking" the sample (i.e. rotating by a fraction of a degree along the θ axis), we can sweep through the Bragg condition, imaging the diffraction pattern at many points as we go, as shown in Fig. 1.3. In reciprocal space, the rotation of the sample corresponds to a rotation of the reciprocal lattice about the illuminating wavevector $\mathbf{k}_i$, which falls on the surface of the Ewald sphere, as shown in Fig. 1.4. Thus the stack of images obtained by rocking the sample actually constitutes a single three-dimensional region of reciprocal space—a 3D diffraction pattern, proportional to the Fourier transform of the 3D sample.

This three-dimensional encoding of both shape and atomic displacement is unique to Bragg diffraction, making BCDI an ideal tool for probing strain. Furthermore, assuming a perfect measurement system (more on that in the next section), the smallest feature that can be resolved with CDI is limited by the illuminating wavelength [21]. Because BCDI uses X rays ($\lambda \sim 0.1$ nm), this puts it firmly in range of the elusive mesoscale, with the potential for atomic resolution.

The Bragg diffraction pattern can be approximated in the far field as a Fourier transform of the

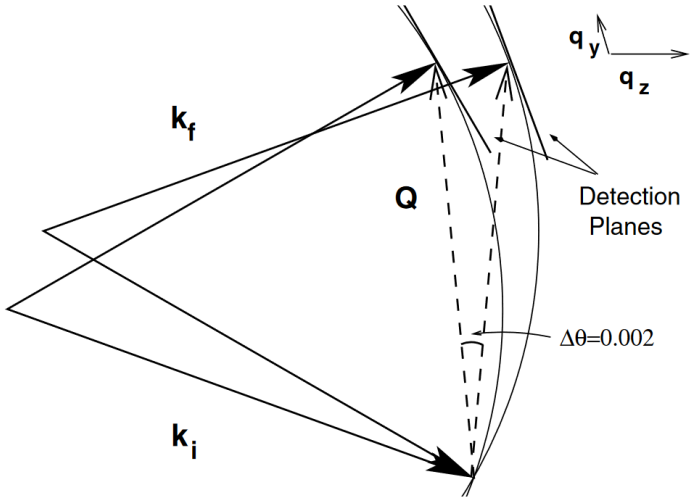

Figure 1.4 A diagram showing the effect of sample rotation on the geometry of reciprocal space. In this reference frame, the reciprocal lattice is assumed to be held constant, causing the Ewald sphere itself to rotate about the point where $\mathbf{k}_i$ touches the Ewald sphere. The scattering vector, labeled **Q** in this diagram, is notated as **q** elsewhere in this document. Figure taken from [11].

exit wave [22],

$$\Psi(\mathbf{q}) = \mathscr{F}[\psi(\mathbf{r})] = \mathscr{F}\left[\rho(\mathbf{r})e^{i\phi(\mathbf{r})}\right]. \tag{1.3}$$

The exit wave's modulus $\rho(\mathbf{r})$ is a measure of the reflectivity of the sample space, and is directly proportional to the electron density of the sample itself. Assuming that the Bragg condition for the region of interest is only satisfied by the sample itself, $\rho(\mathbf{r})$ should be approximately constant within the sample, and zero everywhere else—in other words, it represents the sample's shape. The exit wave's phase $\phi(\mathbf{r})$ represents the projection

$$\phi(\mathbf{r}) = \mathbf{u}(\mathbf{r}) \cdot \mathbf{G} \tag{1.4}$$

where $\mathbf{u}(\mathbf{r})$ is the atomic displacement field and **G** is the normalized *hkl* scattering vector for that particular Bragg peak. This is a subtle simplification of the phase factor given in Eq. (1.2), where the displacement field is projected onto the exact scattering vector **q**. It is allowed since the variations in **q** are very small over the scanning region.

In theory, back-propagating the light to the object plane is as simple as taking the inverse Fourier transform of Ψ. However, since an image detector measures only the intensity of light rather than its amplitude and phase, more advanced techniques are required [23]. The most common of these is iterative phase retrieval (IPR), which involves propagating a trial object back and forth between the real and Fourier domains, applying constraints at both ends [16, 17, 24–26].

1.3 Multipeak BCDI

Each peak only contains information about the atomic displacement field projected along the scattering vector $\mathbf{G}$. Therefore obtaining the entire strain field within the sample requires combining the reconstructed objects of at least three linearly independent Bragg peaks [15, 16, 27]. As a first attempt, one might want to simply combine the final objects of three peak reconstructions, aligning them based on their shared shape. However, due to the size of the phase retrieval search space, the number of local optima, the inherent limitations of digital measurement, and the difficulty of properly aligning independent reconstructions, this approach often comes with a high uncertainty [28].

A better approach known as coupled phase retrieval (CPR) has recently been developed, in which the reconstructing peaks are allowed to share information [28–31]. Instead of finding an optimal phase field $\phi(\mathbf{r})$ for each diffraction pattern, CPR methods seek to find an optimal displacement field $\mathbf{u}(\mathbf{r})$ for the whole set of diffraction patterns. The additional constraints thus placed on the optimization process lead to greater agreement between peaks and help to prevent stagnation. It has even been shown that diffraction patterns which do not reconstruct by themselves can still be part of a convergent CPR optimization, as they receive support from the other peaks [29].

Because each peak represents a unique experimental geometry, it necessarily also has a unique, non-orthogonal coordinate system on which a regular sampling grid is imposed. This presents a problem for CPR, as the various peaks must all update a single amplitude $\rho(\mathbf{r})$ and displacement

field $\mathbf{u}(\mathbf{r})$. In order to account for this, either (1) the data must be resampled onto a common grid compatible with $\mathbf{r}$, or (2) $\rho(\mathbf{r})$ and $\mathbf{u}(\mathbf{r})$ must be resampled onto the coordinates of each peak. Depending on the circumstances, either of the two methods may be preferable. The first requires only one interpolation at the beginning of the reconstruction, and is therefore the computationally cheaper option. However, it also inevitably introduces errors into the data being used for optimization. The second option preserves the fidelity of the raw data, but requires a new resampling to be calculated for each peak, each time ρ and $\mathbf{u}$ are updated.

1.4 Scanning Laue orientation mapping

One of the most difficult aspects of BCDI is finding the Bragg peak in the first place. A typical experimental setup consisting of a 3 cm $\times$ 3 cm detector placed at a distance of 0.5 m from the sample measures less than 0.1% of the 4π steradians of the Ewald sphere, itself only a thin slice of reciprocal space. This is further complicated by the fact that the vast majority of reciprocal space contains information well below the noise threshold of current experiments, with only the immediate volume around each reciprocal lattice point containing measureable intensity.

If the structure and initial orientation of the crystal are known, finding Bragg peaks becomes a matter of calculation. Thus, methods of determining crystal orientation are of the utmost importance to BCDI. Perhaps the most common such method is electron back-scatter diffraction (EBSD) analysis. However, EBSD is a type of scanning electron microscopy, and therefore must be done separately from the BCDI experiment. Therefore, in addition to any errors in the measurement itself, the orientation's accuracy is limited by the act of moving the sample from one system to another.

Scanning Laue orientation mapping is a more recently developed technique which shares most of the same apparatus as the BCDI experiment. It involves illuminating the sample with a large bandwidth of X rays (referred to as a "pink" beam) and measuring the reflection on a large area

detector placed very close to the sample. Because the incident/reflected photon energy defines the Ewald sphere's radius, the large-bandwidth pink beam is able to access a much wider range of peaks than a monochromatic beam. This, combined with the large solid angle subtended by the detector, makes it possible to detect many peaks simultaneously. The relative positions of these peaks is then used to calculate the orientation of the diffracting crystal. By focusing the pink beam to a small spot and rastering it over the sample, this method can be used to create a map of grains and their orientations, all while the sample remains mounted in the X-ray beam.

1.5 Overview of Document

Chapter 2 discusses an algorithm I developed for multipeak BCDI which reconstructs significantly faster than existing methods. This is a particularly important accomplishment as it will allow data analysis to keep pace with data production at upgraded coherent X-ray facilities. Chapter 3 describes the Laue diffraction analysis method for making a spatial map of crystal orientations. In Chapter 4, I discuss the future of this project, including my plan to continue this research in a doctoral program. Finally, Appendix A contains brief descriptions of software I have developed in conjunction with this work.

The content in Chapters 2 and 3 of this document is taken from published or submitted research articles. The articles' content has been reformatted to preserve a single enumeration of figures, equations, and citations throughout. However, there may still be minor notational discrepancies between chapters.

Chapter 2

Cyclic-constrained optimization for multipeak BCDI

The following article has been submitted to the journal *Optics Express* under the title "Experimental demonstration of rapid multipeak Bragg coherent diffraction imaging via cyclic-constrained optimization," authored by J. Nicholas Porter, Yueheng Zhang, Ross J. Harder, Barbara Frosik, Wonsuk Cha, Yuan Gao, Garth Williams, Joshua Miller, Nash Karrington, Andres Herrera, Stephan Hruszkewycz, Anthony Rollett, and Richard L. Sandberg.

My contributions to this work are: (1) developing the presented CCO algorithm for multipeak BCDI, (2) implementing that algorithm in Cohere, the standard BCDI software at APS 34-ID-C (see Section A.1), and (3) collecting and analyzing the data here presented.

Abstract

Multipeak (or multi-reflection) Bragg coherent diffraction imaging (BCDI) allows for highly consistent reconstruction of the three-dimensional strain field within nano- and microcrystals. However, the high computational cost of such reconstructions combined with the increasing brilliance of coherent X-ray sources presents a problem: data production is increasingly outpacing data processing and will soon be orders of magnitude faster. To help prevent a bottleneck, we present a multipeak phase retrieval technique for BCDI, based on cyclic-constrained optimization (CCO), designed to minimize both the time and memory required to perform reconstructions. We show that CCO is able to quickly and consistently reconstruct experimentally obtained diffraction patterns from crystals with varying levels of strain.

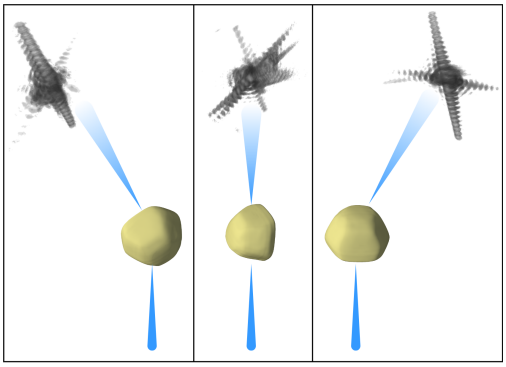

Figure 2.1 Conceptual diagram of a multi-reflection BCDI experiment. Coherent x rays enter from below and interact with the crystal lattice of the sample, producing bright peaks where the Bragg condition is met. While a minimum of three mutually orthogonal peaks are required to reconstruct the strain field, there is no upper limit to the number of peaks.

2.1 Introduction

Bragg coherent diffraction imaging (BCDI) is a rapidly developing field of lensless imaging. Like other forms of coherent diffraction imaging, it is based on the retrieval of phase information from spatially oversampled coherent diffraction intensities [17,25,26], which can then be back-propagated to create an image of the diffracting object once phase retrieval is complete. In the case of BCDI, this diffraction pattern is obtained by reflecting coherent X-rays from atomic planes within a crystal, according to Bragg's law [32]. In this geometry, "rocking" the crystal through the Bragg condition in fine angular increments while sampling a Bragg peak is equivalent (in the elastic photon scattering model) to sweeping out a three-dimensional volume of that crystal's reciprocal space [11]. Furthermore, because Bragg diffraction is highly sensitive to the spacing of atomic planes, any variation in that spacing is encoded into the coherent interference surrounding the corresponding Bragg peak. Combining such information from at least three noncoplanar reflections provides a full 3D image of the lattice distortion (and therefore strain) within a crystal with spatial resolution on the order of tens of nanometers [14, 15, 27, 33–44].

In the past few years, several techniques have been proposed for coupled phase retrieval of

multiple Bragg reflections (typically 3–5, but potentially more) Fig. 2.1, and have been shown to improve both the quality and consistency of reconstruction [28–31]. However, worldwide efforts to create brighter coherent X-ray sources have brought the computational cost of such methods into sharp focus. Fourth-generation synchrotrons, based on diffraction-limited storage rings (DLSR) [45–47], will produce orders of magnitude more coherent X-ray flux, resulting in significantly reduced measurement times for BCDI. With such an upgrade, the hours of exposure needed to collect multiple Bragg diffraction patterns will become minutes. In order to prevent a major data processing bottleneck, and to ensure that informed decisions can be made about *in situ* and *in operando* experiments, it is imperative that algorithms exist to analyze such data in near-real time.

Existing coupled phase retrieval techniques can be divided into two broad categories based on whether they approach reconstruction as a single problem or a set of coupled problems. In the first instance, here referred to as global optimization (GO), an advanced forward model is used to define and minimize a single cost function for all diffraction patterns [31]. The GO approach, though powerful, is computationally very expensive, and has yet to be implemented in a viable way for real-time analysis.

In the second approach, each diffraction pattern is phased individually using the single-peak forward model, but an additional "coupling" step ensures that the reconstructing exit waves all agree on underlying physical properties, such as electron density and/or lattice displacement. We refer to this as the constrained optimization approach, and further subdivide it into parallel-constrained optimization (PCO) [28, 30] and cyclic-constrained optimization (CCO) [29]. In PCO, concurrently phased Bragg peaks are brought into agreement every few iterations. In PCO, Bragg peaks are phased in series, each passing its improvements to the next. This serial phasing reduces the memory footprint of the algorithm, as well as the number of parallel processes required. In this letter, we focus on the CCO technique as a good candidate for minimizing the computational cost of multipeak

BCDI thus allowing near-real time multi-Bragg peak phase retrieval. It is worth briefly noting that, based on the cited literature [28–31], we will assume a preference for coupled over uncoupled phase retrieval methods for multipeak BCDI. For a justification of this assumption regarding this particular method, see the Supplemental Information (SI).

2.2 Cyclic-constrained optimization

A constrained optimization problem is one in which some regions of the optimization space are excluded from consideration [48]. For example, consider the reconstruction of a single Bragg peak. The real-space electron density ρ is able to vary freely, but the lattice displacement field $\mathbf{u}$ is subject to the constraint that only its projection along the scattering vector $\mathbf{G}$ may vary, since no information about the orthogonal component is encoded into that diffraction pattern [15]. In practice, this is naturally enforced by optimizing the amplitude A and phase ϕ of the exit wave, assuming the relationships

$$A \propto \rho, \tag{2.1}$$

$$\phi = \mathbf{u} \cdot \mathbf{G}. \tag{2.2}$$

This effectively reduces the dimensionality of each point in space from four (ρ, u_x, u_y, u_z) to two (A, ϕ).

In the CCO approach to multipeak phase retrieval, the problem of finding a ρ- and $\mathbf{u}$-field that fits all the observed diffraction patterns is posed as a set of such constrained optimization problems. Each constrained problem is initialized by projecting the current state of $(\rho, \mathbf{u})$ onto an exit wave (A, ϕ) corresponding to a single Bragg peak. After a small number of phase retrieval iterations, the updated exit wave is, in turn, used to update ρ and $\mathbf{u}$, and the process repeats with a new peak. Because of the dot product in Eq. (2.2), phasing a single peak is only able to adjust the component of $\mathbf{u}$ which is parallel to that peak's $\mathbf{G}$-vector. However, by making many adjustments

along different vectors that collectively span three dimensions, the CCO method is able to address the larger (unconstrained) optimization problem.

An analogy is found in the ptychographic iterative engine (PIE) developed by Rodenburg and Faulkner [49] and later improved by Maiden *et al.* [50, 51], in which diffraction patterns from partially overlapping projections of a single object are phased in series. Each phased projection updates the larger field of view in a way that improves the initial guess for any adjacent projections. Effective but computationally more intense solutions to the ptychography problem have also been developed that adopt a global fitting approach [52], but the PIE approach provides simplicity and speed which led to its widespread use.

Since each reflection is measured in a unique sample orientation, combining them in a consistent way requires some form of resampling [53]. The interpolation inherent in such resampling is an expensive computational process. As such, we opted to resample each diffraction pattern into a common reciprocal-space grid prior to phase retrieval, rather than resampling the reconstruction each time it is projected onto a new peak. This approach drastically reduces the computational cost of reconstruction (by an order of magnitude or more) and simplifies the description of the algorithm by dispensing with the need for transformation operators. Interpolating the raw data before phasing is not without drawbacks—poorly resolved features in the original image are likely to be further misrepresented in the interpolation [54]. However, in a sufficiently oversampled diffraction pattern [55–57], the only features on those scales should be noise.

2.3 Algorithm

It is worth making a brief comment on notation before describing the algorithm in detail. In the interest of simplicity and reproducibility, we have opted for an assignment notation (e.g. $\psi \leftarrow f(\psi)$), which is more akin to how such algorithms are actually implemented in code. Unless otherwise

stated, all operations on arrays are assumed to be element-wise.

Algorithm 1 A superiteration of the CCO algorithm

function SUPERITERATE($\rho, \mathbf{u}, I, \mathbf{G}, \beta, m$)

$\psi \leftarrow \frac{\rho}{|\mathbf{G}|} e^{i(\mathbf{u}\cdot\mathbf{G})}$ ▷ Eq. (2.3)

for m times **do**

$\psi \leftarrow$ PHASERETRIEVAL(ψ, I) ▷ HIO, ER, etc.

$\rho \leftarrow \rho + \beta(|\mathbf{G}||\psi| - \rho)$ ▷ Eq. (2.4)

$\mathbf{u} \leftarrow \mathbf{u} + \beta \frac{(\arg(\psi) - \mathbf{u}\cdot\mathbf{G})}{\mathbf{G}\cdot\mathbf{G}}\mathbf{G}$ ▷ Eq. (2.5)

return $\rho, \mathbf{u}$

The CCO algorithm (Algorithm 1) updates a single 3D array representing a physical object. Each element (voxel) in that array is a 4-element vector $[\rho, \mathbf{u}]$, where ρ is proportional to electron density and $\mathbf{u} = [u_x, u_y, u_z]$ is the lattice displacement field. We then select a diffraction pattern I and corresponding scattering vector $\mathbf{G}$ and apply the relevant optimization constraint by calculating the exit wave

$$\psi \leftarrow \frac{\rho}{|\mathbf{G}|} e^{i(\mathbf{u}\cdot\mathbf{G})}. \tag{2.3}$$

The presence of $|\mathbf{G}|$ in Eqs. (2.3) and (2.4) accounts for the reduced intensity of higher order peaks.

Phase retrieval algorithms such as error reduction, hybrid input-output, shrinkwrap, etc. [17, 25, 26, 58] are then applied to ψ using the corresponding diffraction data. We refer to such a typical phase retrieval iteration here as a "subiteration."

After some number of subiterations, the improved exit wave is used to update the shared object using a weighted average. In the case of ρ, this is fairly straightforward:

$$\rho \leftarrow \rho + \beta(|\mathbf{G}||\psi| - \rho), \tag{2.4}$$

where β is a weighting parameter. In the case of $\mathbf{u}$, we need to take into consideration the fact that the phase of a Bragg reflection only contains information about the displacement field parallel to

the scattering vector $\mathbf{G}$:

$$\mathbf{u} \leftarrow \mathbf{u} + \beta \frac{(\arg(\psi) - \mathbf{u} \cdot \mathbf{G})}{\mathbf{G} \cdot \mathbf{G}} \mathbf{G}. \tag{2.5}$$

The entire process described to this point constitutes a single "superiteration," and is summarized in Algorithm 1. At this point, a new peak is selected, and the process repeats.

We integrated our CCO technique for multipeak BCDI into Cohere, a freely available Python-based software developed at APS beamline 34-ID-C. This implementation introduces several key differences compared to the previously published CCO algorithm [29]. First, the cycle of peaks now uses random rotations, departing from the fixed rotation used before. Second, the number of subiterations per superiteration has been increased from one to five. Third, we now combine information about the displacement field into the shared object at each superiteration. The previously published CCO implementation [29] featured superiterations that didn't update the displacement field, but instead stored the phase in memory to be used the next time that particular peak was treated. Lastly, we have introduced a weighting parameter β, which warrants further discussion.

If the diffraction data were perfect, the weighting parameter could be set to $\beta = 1$ (entirely favoring each new update) for the duration of the reconstruction. In practice, however, data often contain artifacts such as shot noise or stray reflections from other crystals. These cause the constrained optimizations to disagree, often slightly, but sometimes significantly. With β set to unity, the shared object will develop very quickly, but it will always prefer the most recently phased reflection, artifacts included. By contrast, a β closer to zero will update the shared object more slowly, but will prefer features that are common among the different datasets. With this in mind, we chose to have a high β for most of the reconstruction, then gradually taper it to zero toward the end. This seems to work well for the crystals we have imaged ($\sim$ 500 nm Au particles with an FCC structure), though we have not looked closely at other potential strategies.

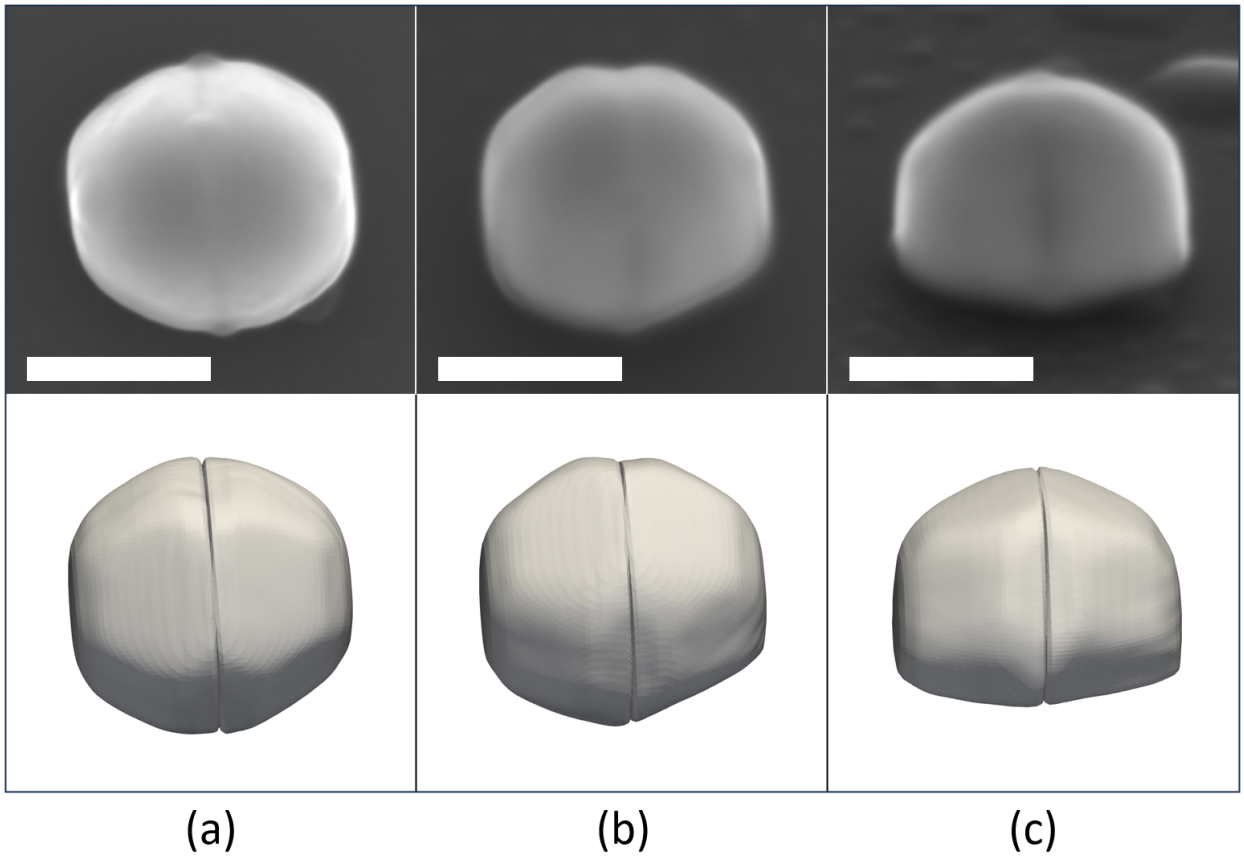

Figure 2.2 Comparative images of both halves of a Au bicrystal, viewed at (a) 0°, (b) 30°, and (c) 60° from normal incidence. The top row shows images taken by an SEM; the bottom row shows a 60%-density isosurface of the CCO reconstruction. In all six images, grain A is on the left. Scale bars indicate 500 nm.

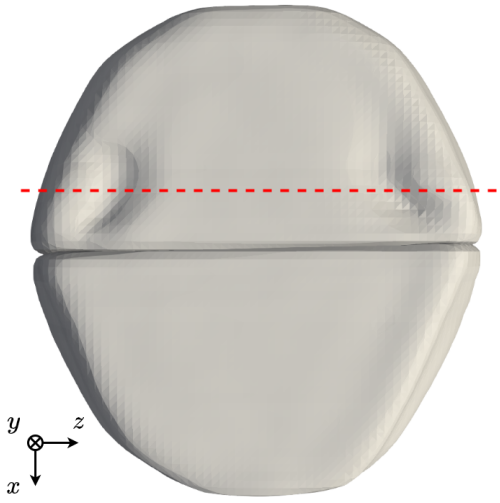

Figure 2.3 Underside of the reconstructed Au grains, with grain A on top. From this view, there are two clear deformations in the isosurface of grain A. The dotted line indicates the position of the cross-section shown in Fig. 2.4.

2.4 Results

To test the efficacy of our CCO method, we measured coherently scattered Bragg peaks from a dewetted gold (Au) nanocrystal grown on a single crystal Niobium doped strontium titanate substrate at the 34-ID-C beamline at the Advanced Photon Source. The CCO method was used to separately reconstruct two halves (hereafter called grains A and B) of a twinned Au bicrystal, shown in Fig. 2.2. The crystallographic relationship between grains A and B was that of a coherent twin pair with a 60° rotation in a shared 111-family lattice plane. Scanning Laue diffraction analysis [59–61] was used to determine the orientation of the two grains, from which the diffraction conditions of the $1\bar{1}1$, $0\bar{2}0$, $1\bar{1}\bar{1}$, 200, and 002 peaks of grain A and the $\bar{2}00$, $\bar{1}\bar{1}1$, $0\bar{2}0$, $1\bar{1}1$, and 002 peaks of grain B were determined. The diffraction patterns were measured on an ASI Quad (512x512) Timpix detector, using 10 keV photon energy monochromatized to $\Delta E/E = 10^{-4}$. In the resulting reconstructions, the edge length of each voxel in the reconstructions of grains A and B are 10.0 nm and 9.9 nm, respectively. The two reconstructions were aligned by eye.

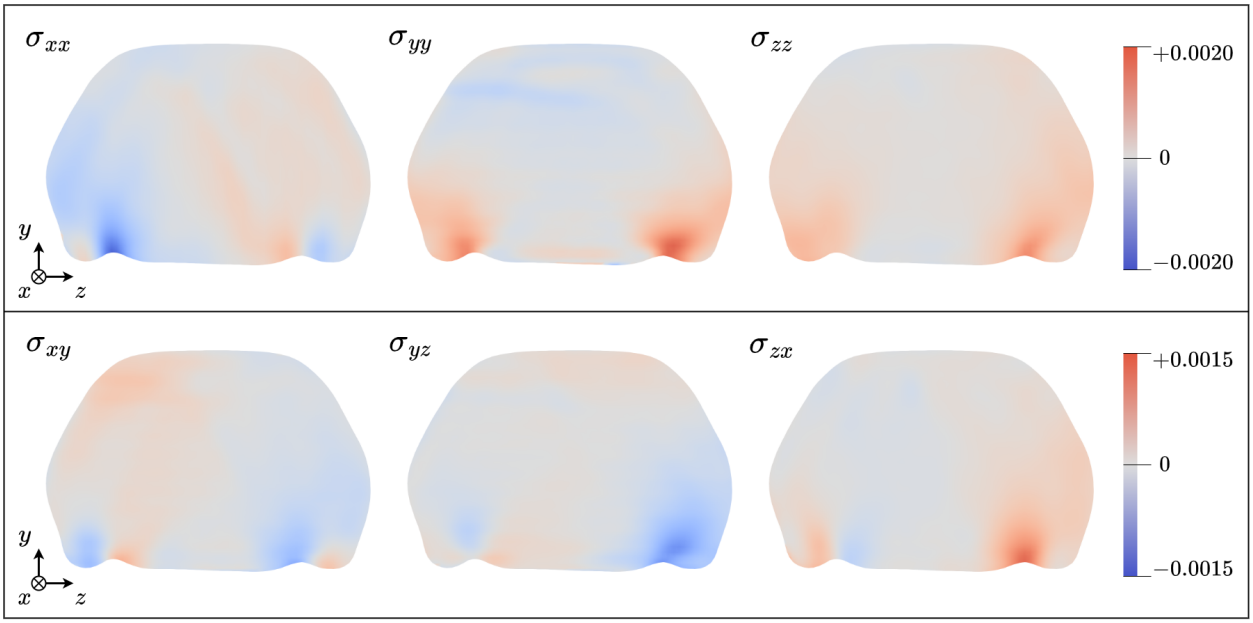

Figure 2.4 Cross section of grain A, showing each of the six (unitless) strain components—volumetric on the top row, shear on the bottom. The cross section was placed so as to cut through the middle of the two deformations on the bottom of the crystal, as shown in Fig. 2.3.

Of particular note in the reconstruction are two large deformations along the bottom face of grain A, shown in Fig. 2.3. Similar features have appeared on a number of reconstructions of the same type of sample and may indicate an imperfect coupling between the gold crystals and the strontium titanate (STO) substrate. From the cross section in Fig. 2.4, it is clear that both deformations are significant sources of internal strain. It is worth emphasizing that multipeak BCDI is uniquely able to resolve these features. Their position on the underside of the crystal makes them invisible to scanning electron microscopy. A single-peak BCDI reconstruction would reveal their existence, but would only provided limited information about the associated strain. Multipeak BCDI is able to provide high-resolution imaging of the full strain tensor.

The recipe used to reconstruct each grain was an alternating 180 subiterations of HIO and 20 of ER, repeated five times for a total of 1000 subiterations (200 superiterations). After each subiteration (both HIO and ER), shrinkwrap was applied using a gaussian ($\sigma = 1$ pixel) filtered amplitude profile

and a cutoff threshold of 20% [26]. The weighting parameter was set at $\beta = 1$ for the first 750 subiterations, then gradually decreased to a final value of $\beta = 0$ over the last 250 subiterations. To avoid artifacts caused by phase wraps, strain was calculated using a phase-differentiation technique demonstrated by Hofmann *et. al* [44].

The reconstruction was done on an Intel Xeon (Ivy Bridge) processor, with the majority of the computation performed on a Nvidia RTX A4500 graphics card. It should be noted that, due to its inherently serial nature, CCO phase retrieval is not easily amenable to parallel computing beyond GPU acceleration of array operations. After resampling, the diffraction patterns were cropped/padded so that each was a $240 \times 240 \times 240$ array. Reconstructing five peaks of this size used less than 6 GB of VRAM, well within the capacity of even mid-level GPUs, and the entire process took less than 5 minutes (100 seconds of phasing, 176 seconds of pre- and post-processing). Thus, our CCO method solves the problems of data analysis bottlenecks at DLSR sources wishing to perform multipeak BCDI.

To measure consistency, the reconstruction was repeated 50 times for each grain, the best of which is shown in Figs. 2.2 and 2.4. Because its internal structure contained minimal strain, grain B was the easier reconstruction, with all 50 attempts converging to the same density and strain fields and only three containing a significant artifact (small region of missing density, which typically fills in after continued phasing). However, even the more highly strained grain A only failed to converge once, with an additional six attempts containing artifacts similar to the aforementioned. Additionally, the 50 reconstructions for each grain were used to calculate a phase retrieval transfer function (PRTF) [13, 62], shown in Fig. 2.5. Using $1/e$ as a standard, the PRTF shows 20.7 nm resolution for grain A and 17.9 nm resolution for grain B.

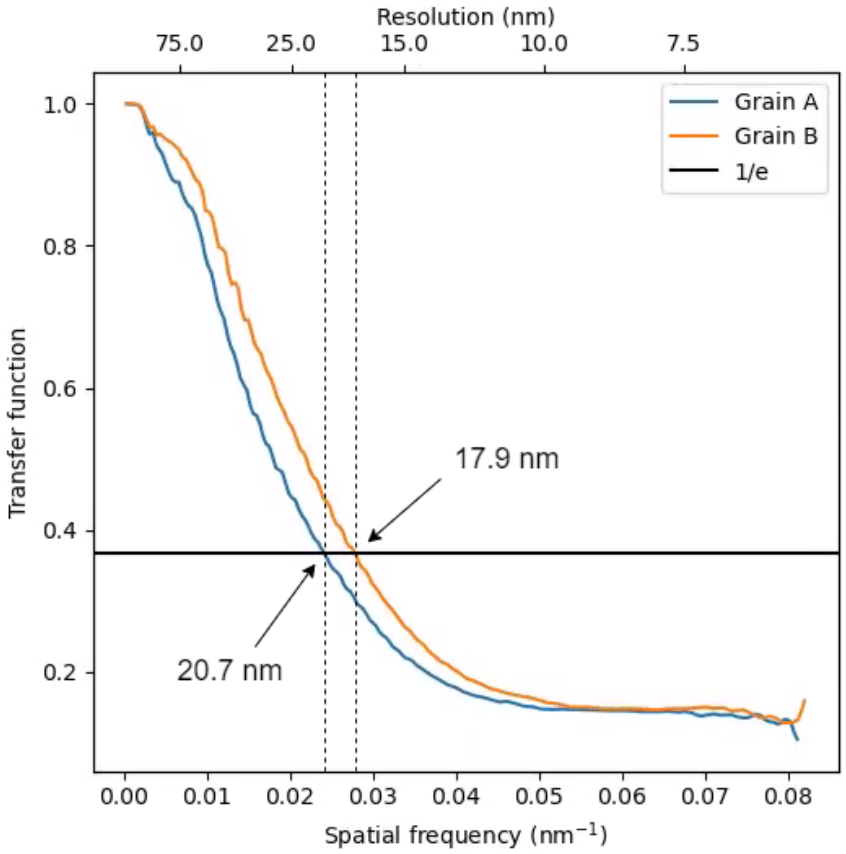

Figure 2.5 Phase retrieval transfer functions (PRTF) for both grains across 50 reconstructions, with a reference line at $1/e$. The point where the PRTF crosses $1/e$ defines the resolution of the corresponding reconstructions.

2.5 Conclusion

This experimental demonstration of CCO as a rapid, memory-efficient, and robust reconstruction method is important for near-real time analysis of multipeak BCDI data at upgraded beamlines worldwide. By relying on the single-peak forward model, it is able to take full advantage of the efficiency of such algorithms as HIO and ER. By phasing peaks in series rather than parallel, it eliminates the need for multiple GPUs. By resampling the data rather than the reconstruction, we further reduced both the conceptual and computational complexity of the multipeak problem. Beyond efficiency, we have demonstrated that CCO provides the highly consistent reconstructions characteristic of multipeak BCDI.

2.6 Supplemental document

2.6.1 Use of the term “exit wave"

In its purest sense, the term “exit wave" refers to the complex electromagnetic field that occurs immediately after a coherent beam interacts with a sample. In most forms of coherent diffraction imaging (CDI), the computational array representing the sample in direct space is simply a discretization of this field. Thus, the term is often used interchangeably to refer to both the physical field and the computational array. This usage has, for better or worse, spread to contexts in which the relationship between the field and the array is more complicated.

For example, in Bragg coherent diffraction imaging (BCDI), the sample is rotated through the Bragg condition, and the beam-sample interaction forms a series of unique exit waves. Each exit wave then propagates to a detector plane, where it is measured as an image. These images are then stacked into a single 3D array referred to simply as “the diffraction pattern.” despite being a compilation of many different formed at slightly different geometries Similarly, the Fourier

inversion of this array is commonly called "the exit wave," even though it does not necessarily represent any of the individual exit waves that formed the 2D slices.

This article follows the above convention, referring to the computational arrays as diffraction patterns or exit waves. Both terms leverage familiar concepts from other forms of CDI to quickly and efficiently inform the reader of the computational role that each array plays in the algorithm. Even so, we acknowledge that it is often important to use more explicit terminology to specify whether a computational array is a direct representation of a physical field.

2.6.2 Comparison with uncoupled methods

This article takes for granted that coupled methods are preferred over uncoupled ones for reconstructing strain fields from multiple Bragg diffraction patterns. This is supported by comparative analysis for all existing coupled phase retrieval techniques [28–31]. However, in the interest of completeness, we present the following.

In order to fairly compare the CCO algorithm to uncoupled multipeak BCDI, we use both methods to perform reconstructions with only four of the five measured peaks for each grain. The obtained density and displacement fields is then projected onto an exit wave corresponding to the excluded peak and propagated into the Fourier domain. The resulting diffraction amplitude can then be compared to the "control peak" to determine how accurately the reconstruction fits the data. We performed 30 such reconstructions for each peak of each grain, using both CCO and uncoupled techniques. The diffraction datasets used for the CCO reconstructions were resampled onto a common grid (see main text). In order to fairly test the convergence properties of the algorithms, the same resampled data was also used for the uncoupled reconstructions.

One immediate difference between the two methods is that a few coupled reconstructions (10 out of 300) altogether failed to produce any recognizable object, a phenomenon which did not occur with the uncoupled technique. One possible explanation is that, for a sufficiently bad initial guess,

Metric	Coupled (CCO)	Uncoupled	Winner	Margin
SSIM	0.98779	**0.99154**	Uncoupled	0.380%
PSNR	46.681	**46.682**	Uncoupled	0.002%
NRMS	**102.68**	103.95	Coupled	1.220%
χ^2	**10655**	10916	Coupled	2.393%
NMI	**0.31266**	0.21079	Coupled	48.328%
EHD	$\mathbf{8.39 \times 10^{-5}}$	1.16×10^{-4}	Coupled	27.521%
EHD (log)	$\mathbf{8.53 \times 10^{-2}}$	1.04×10^{-1}	Coupled	17.606%

Table 2.1 A comparison of how well the CCO and uncoupled BCDI methods were able to reconstruct the amplitude of a control peak, based on a variety of metrics. Note that SSIM, PSNR, and NMI are similarity metrics, while NRMS, χ^2, and EHD (see Eq. (2.7)) are difference metrics. For each of the 10 peaks examined, 30 reconstructions were performed, 4 of which (those with the highest EHD) were excluded from this analysis. Thus, each number represents an average over 260 reconstructions.

the information lost during coupling exceeds the information recovered in a superiteration. If such is the case, then the serial coupling inherent to the CCO technique inadvertently creates a small but non-negligible possibility of a cascading failure. However, due to the rarity of these cases, we will leave the mitigation of such failures for another discussion and restrict our comparison to successful reconstructions.

We compared the reconstructed diffraction patterns to the control peaks with a variety of metrics, including structural similarity index measure (SSIM) [63], peak signal-to-noise ratio (PSNR), normalized root-mean-square error (NRMS), chi-square error (χ^2), and normalized mutual information (NMI) [64, 65]. The results of this analysis, averaged over many reconstructions, are given in Table 2.1. Interestingly, of the metrics hitherto mentioned, only the NMI was significantly different between CCO and uncoupled reconstructions. As such, it's worth examining the concept of mutual information.

The NMI metric was developed for medical image registration. To quote from Feixas *et al.*, [66], "the basic idea behind [information-based similarity metrics] is that two values are related (or similar) when there are many other examples of those values occurring together in the overlapping image volume." In other words, the similarity of two images is related to how often voxels of similar amplitude in one image tend to also have similar values in the other. More quantitatively, the normalized mutual information between two images X and Y is a number on the range $[0,1]$, defined as

$$\mathrm{NMI}(X,Y) = \frac{H(X)+H(Y)}{H(X,Y)} - 1, \tag{2.6}$$

where $H(X)$ and $H(Y)$ are the respective marginal entropies of X and Y, and $H(X,Y)$ is their joint entropy [65]. These entropies are calculated by using a histogram to estimate the appropriate probability density functions, $p(x)$, $p(y)$, and $p(x,y)$ [64]. Because the NMI is based on information content rather than pixel-wise error, it is a powerful metric for aligning images with differing modalities. However, that same flexibility is potentially problematic in the present application, where we don't just want to show that there is some arbitrary relationship between the two images, but that they are actually the same.

In order to confirm such a relationship, we must more closely examine the joint probabilty density function itself. As before, this may be approximated with a 2D histogram. Furthermore, different insights can be gained by considering both an equal-bin as well as a log-bin histogram. This is because such a large number of the pixels in a typical diffraction pattern have intensities toward the very low end of the dynamic range, and the logarithmic spacing of bins allows for finer distinction between these low intensities. Figure 2.6 shows some of these histograms, calculated for grain A with the (002) peak used as control. We may then calculate an expected histogram deviation (EHD) from the main diagonal,

$$\mathrm{EHD}(X,Y) = \frac{\sqrt{2}}{N}\sum_{i,j}|i-j|(P(X,Y))_{i,j} \tag{2.7}$$

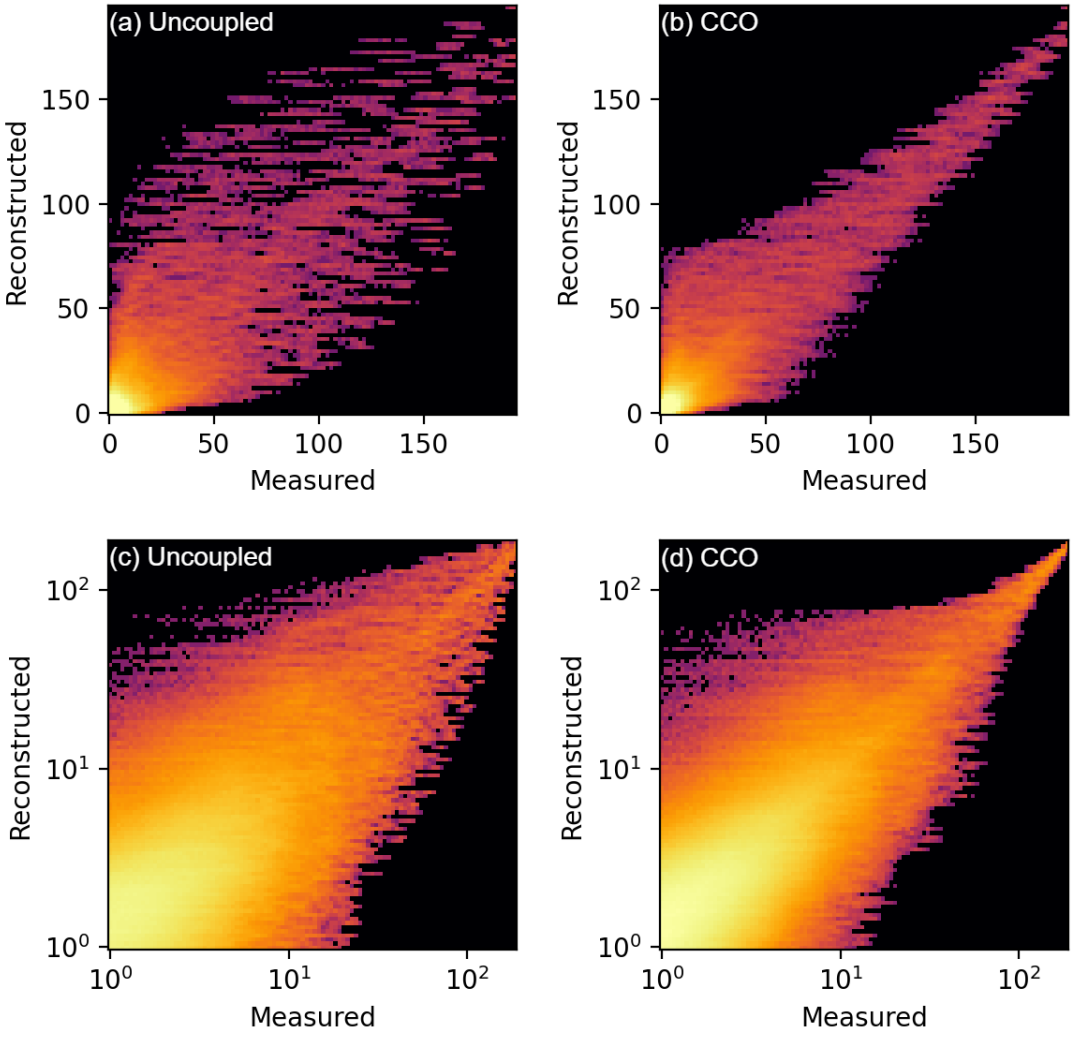

Figure 2.6 Joint histograms comparing the measured and reconstructed amplitudes of the (002) diffraction peak of grain A. Plots (a) and (b) represent the uncoupled and CCO reconstructions, respectively. Plots (c) and (d) were calculated using the same reconstructed images, but with logarithmically spaced bins.

where N is the number of bins along each side, i and j represent the indices of each bin in the histogram, and $P(X,Y)$ is the 2D histogram array. For the equal-bin histogram, this is equivalent to the expected deviation of the two images from their element-wise mean. For the log-bin histogram, the meaning is similar, but measures the expected relative deviation from the geometric mean. The equal-binned and log-binned EHD for the aforementioned reconstructions are also given in Table 2.1.

It remains unclear why the SSIM, PSNR, NRMS, and χ^2 metrics were all unable to find a significant difference between the uncoupled and CCO methods. However, the combination of the NMI and EHD metrics provides a strong argument for including the present CCO method among other successful coupled phase retrieval methods for multipeak BCDI.

Chapter 3

Crystal orientation mapping via scanning Laue diffraction analysis

The following article appeared in *The Journal of Synchrotron Radiation* under the title "Mapping nanocrystal orientations via scanning Laue diffraction microscopy for multi-peak Bragg coherent diffraction imaging." My primary contributions to this work are: (1) programming computationally efficient routines for image pre-processing, and (2) developing the concept from a few disorganized Python scripts into a usable software application (see Section A.2). The original article also includes a supplemental document, which can be found online.

Full citation:

Y. Zhang, J. N. Porter, M. J. Wilkin, R. Harder, W. Cha, R. M. Suter, H. Liu, L. Schnebly, R. L. Sandberg, J. A. Miller, J. Tischler, A. Pateras, and A. D. Rollett, "Mapping nanocrystal orientations via scanning Laue diffraction microscopy for multi-peak Bragg coherent diffraction imaging," *J Synch. Rad.* **30**, 796–806 (2023).

Abstract

The recent commissioning of a movable monochromator at the 34-ID-C endstation of the Advanced Photon Source has vastly simplified the collection of Bragg coherent diffraction imaging (BCDI) data from multiple Bragg peaks of sub-micrometre scale samples. Laue patterns arising from the scattering of a polychromatic beam by arbitrarily oriented nanocrystals permit their crystal orientations to be computed, which are then used for locating and collecting several non-co-linear Bragg reflections. The volumetric six-component strain tensor is then constructed by combining the projected displacement fields that are imaged using each of the measured reflections via iterative phase retrieval algorithms. Complications arise when the sample is heterogeneous in composition and/or when multiple grains of a given lattice structure are simultaneously illuminated by the polychromatic beam. Here, a workflow is established for orienting and mapping nanocrystals on a substrate of a different material using scanning Laue diffraction microscopy. The capabilities of the developed algorithms and procedures with both synthetic and experimental data are demonstrated. The robustness is verified by comparing experimental texture maps obtained with Laue diffraction microscopy at the beamline with maps obtained from electron back-scattering diffraction measurements on the same patch of gold nanocrystals. Such tools provide reliable indexing for both isolated and densely distributed nanocrystals, which are challenging to image in three dimensions with other techniques.

3.1 Introduction

Understanding the relationship between macroscopic mechanical properties of materials and their nanoscale structure is a long-term endeavor. Theoretical models of phenomena such as twin formation and dislocation motion require three-dimensional (3D) experimental validation at the nanoscale [1, 67–69]. Bragg coherent X-ray diffraction imaging (BCDI) has emerged as a strong candidate for such experiments. This non-destructive technique provides 3D images of lattice strain fields in nanocrystals with resolution approaching sub-10 nm and even allows operando imaging of defects [70]. Upgrades to X-ray light sources in the coming years will enable BCDI at sub-nanometre resolution and may enable near atomic resolution of these strain fields (https://www.aps.anl.gov/APS-Upgrade/About-the-APS-Upgrade).

In BCDI, a nanocrystal is illuminated by a monochromatic, coherent X-ray beam. 3D real space images of the crystal electron density are enabled by collecting the 3D reciprocal space intensities of the coherently scattered Bragg peak during a rocking scan measurement. A detector records a series of two-dimensional (2D) slices of the 3D Bragg peak at each angular step in the far-field [71]. The 3D intensity distribution of the coherent X-ray diffraction pattern is then reconstructed via iterative phase retrieval algorithms to yield the real space electron density of the crystal [17, 25]. The real-space electron density is a complex function whose phase contains the projection of the coarse-grained lattice displacement along the scattering vector. To recover the full strain tensor of the crystal at least three BCDI data sets from linearly independent Bragg reflections are needed [35, 72].

Recent methods for coupled reconstructions from multiple Bragg reflections of the same nanocrystal provide the full strain tensor in every volume element or voxel of the reconstructed volume [30, 72]. In previous work published by Newton *et al.*, knowing the growth direction of a ZnO nanorod and finding one (101) reflection allowed an orientation matrix to be derived and BCDI datasets from six different reflections to be recorded for the first time [35]. In the work of

Hofmann *et al.*, in which they measured multiple Bragg peaks from the same isolated nanocrystal, the crystal orientation was determined beforehand using broadband Laue diffraction at another instrument [72]. Yang *et al.* demonstrated that the orientation of exposed nanocrystals can be found using electron back-scatter detection (EBSD), which could then be used to align the crystal for BCDI experiments [73]. While that work shows the potential of EBSD to pre-determine the crystal orientation for subsequent BCDI measurements, it only provides orientations of grains whose top surface is accessible for electron diffraction because electron penetration into metals at 70° incidence is limited to a few nanometres. For efficient determination of crystal orientations of buried nanocrystals, or pairs of neighboring grains in a 3D polycrystalline material, one needs a method to determine orientations in situ. This is especially true if multi-peak BCDI is to be applied to in situ deformation experiments such as tensile or compressive loading where grains may move and rotate making the tracking of multiple Bragg peaks in reciprocal space impossible without repeated Laue orientation mapping at the same beamline.

Laue microscopy is a powerful tool for investigating local crystal structure and microstructural evolution during deformation, thermal expansion and other strained states [74–76] which uses a Pt wire to scan through the diffraction signal near the sample to probe the depth origin of each diffracted beam by correlating blocked reflections with the location of the wire. Additionally, pencil-beam Laue diffraction tomography has been demonstrated using a tomographic approach for the 3D reconstruction [77]. Even though these methods provide elastic strain mapping, they are challenging to combine with BCDI and do not currently reach significantly sub-micrometre spatial resolution in 3D. Combining BCDI with micro-Laue diffraction microscopy provides high spatial and orientation resolution with reasonable acquisition times, i.e. using Laue microscopy to determine the orientation of multiple grains in a polycrystal, acquire multiple BCDI peaks from each grain and reconstruct the 3D shapes and strain fields with sub-10 nm resolution. The existing Laue diffraction microscopy at 34-ID-E uses DAXM with ray-tracing analysis to register the resulting

diffracted signals to their corresponding depths to achieve depth resolution [76]. The double-crystal Si (111) monochromator at beamline 34-ID-E enables fast switching between monochromatic and polychromatic modes, with energy tunable between 7 and 30 keV. The sample is scanned using a precise three-axis stage, positioned at a 45° angle to the incoming X-ray beam for a sample depth range of approximately 100 μm. Laue patterns are captured by a Perkin-Elmer pixel-array detector (409.6 mm × 409.6 mm, 2048 × 2048 pixels, 16-bit dynamic range), mounted in a 90° reflection geometry approximately 500 mm above the sample. The detailed experimental geometry can be found in the work of Liu *et al.* [78]. The resulting overlapping Laue patterns generated within each subgrain volume along the microbeam are reconstructed and indexed using *LaueGo* (written in C and Igor Pro), which was utilized for routine operations of the 3D X-ray Laue diffraction microscope at the E hutch of sector 34-ID [78].

Recently, the 34-ID-C beamline of the Advanced Photon Source integrated a movable monochromator, which allows switching between a monochromatic X-ray beam used for BCDI and a polychromatic (pink) beam used for Laue diffraction. Laue diffraction allows users to determine individual crystal orientations at the beamline in the laboratory frame and has greatly simplified multi-reflection BCDI at 34-ID-C [59].

To acquire an orientation map of many crystals, it is essential to automate indexing methods for scanning Laue diffraction microscopy. Here, we demonstrate such an automated workflow that executes the required Laue diffraction analysis, taking a scanning Laue diffraction dataset and returning an orientation map of the sample akin to EBSD. This technique can be used to rapidly select crystals for BCDI measurement, increasing the potential experimental throughput while at a beamline.

To extend the Laue orientation methods to polycrystalline samples and acquire an orientation map in a fashion similar to existing Laue diffraction microscopy at 34-ID-E [76], several tools had to be developed to automate the Laue analysis for the measurements performed at 34-ID-C.

In previous work, we demonstrated Laue diffraction microscopy at 34-ID-C for orienting a single isolated gold nanocrystal [59]. In that work, the software package *LaueGo* was used to index Laue patterns [78]. However, the precision of indexing arbitrarily oriented nanocrystals was only 0.2°. This error originated in the calibration of the detector position and orientation. In addition, the procedure of identifying the Bragg peaks that belong to the same single nanocrystal required manually moving the monochromator crystals in and out of the pink X-ray beam. We discuss the various experimental modalities in Section 2.1[link]. To implement a fully automated Laue microscopy capability at 34-ID-C several analysis components had to be developed to deal with the unique features of the Laue diffraction measurement at 34-ID-C. First, the closer proximity between the sample and detector at 34-ID-C ($\sim$ 25 mm) compared with 34-ID-E ($\sim$ 500 mm) hinders the use of a scanning differential aperture for depth resolution, thus increasing the difficulties of indexing overlapping Laue diffractions. Second, contrary to 34-ID-E, the photon-counting Eiger2 detector exhibits a very different noise variation than that seen at 34-ID-E.

There are several reasons for the difference in the noise between the Eiger2 and the Perkin-Elmer detector. First, the Perkin-Elmer detector at 34-ID-E is mounted relatively far (500 mm) from the beam/sample interaction point. Therefore, the non-crystallographic scattering is nearly uniform across the detector face. Additionally, the Perkin-Elmer is not photon counting and displays significantly less variation in detected photon density across the detector surface. 34-ID-E uses a simple threshold to isolate peaks from the near uniform background on the Perkin-Elmer. At 34-ID-C the photon-counting detector (Eiger2) is much closer to the sample ($\sim$ 67 mm). The background scattering is therefore non-homogeneous across the detector. Near the center of the detector the background is nearly 1000 photons/s whereas at the edges it drops down to around 400 photons/s. The dimmer peaks in the Laue pattern can be as low as 400 photons/s. Therefore, a simple threshold does not work, because the dimmer peaks near the edges would be eliminated by the higher threshold value. This motivates the effort to subtract a spatially variable background.

At 34-ID-E the standard workflow is designed for samples composed of a single material. At 34-ID-C (i.e. this work) two materials are typically present, i.e. nanocrystals atop a crystalline substrate. Typical combinations are silicon or SrTiO3 (STO) for the substrate with gold or platinum nanocrystals. The standard workflow at 34-ID-E is not intended for indexing Laue patterns with multiple materials simultaneously, especially not where the phase of interest has far weaker peaks than the substrate. The 34-ID-C workflow segments all the peaks, separates out the substrate peaks from those of the nanocrystals and indexes them separately. Additionally, we learned quickly that the movable monochromator implemented for this project did not have a reliable energy calibration curve. As a result, the detector calibration methods developed at 34-ID-E could not be used as-is to refine the relevant parameters [76]. Thus, developing a new workflow was required for detector calibration, background subtraction and automatic peak identification in the recorded Laue patterns.

3.2 Scanning Laue diffraction microscopy

3.2.1 Experimental modalities

A schematic of the experimental geometry is shown in Fig. 3.1(a). The sample is placed on top of a piezo stage with three degrees of freedom of rotation (angles θ, ϕ, χ) and three degrees of freedom for translation (axes x, y, z). Two different detectors are used for recording Laue patterns and coherent diffraction patterns. The Laue detector (Eiger2) is aligned such that its front surface is facing outboard of the synchrotron from the inboard side of the beam. This detector can move in y up or down vertically and in x inboard/outboard away/towards from the sample but is fixed in z. The detector used for collecting BCDI datasets is attached to the diffractometer arm and has three degrees of freedom. The distance of this detector from the sample can be varied within the range 0.5–2.5 m while the arm allows rotation about the x and y axes, angles γ and δ, respectively, as defined in Fig. 3.1(a). With a prior knowledge of the energy bandwidth in the beam and symmetry of

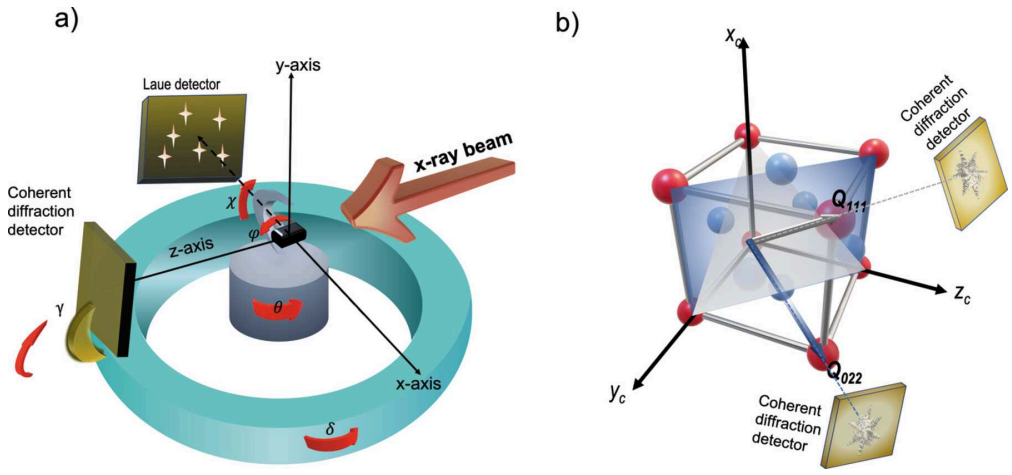

Figure 3.1 (a) Schematic of the experimental geometry at the 34- ID-C beamline. Rotations in (a) are shown at one diffractometer snapshot; when the sample stage is rotated to $\theta = 0°$, $\phi = 0°$ and $\chi = 90°$ and the BCDI detector is rotated to $\gamma = 0°$, $\delta = 0°$. At $\theta = 0°$, the incident beam is perpendicular to the detector surface when the detector is sitting at $\delta = 0°$ and $\gamma = 0°$. At $\chi = 90°$ and $\phi = 0°$, the surface normal of the sample is parallel to the y-axis. The diffractometer is as specified in the Spec Sixc mode [79]. The incident X-ray beam is antiparallel to the z-axis of the laboratory frame. The Laue detector is shown with its surface being normal to the x-axis of the laboratory frame; the x-axis points towards the outboard of the synchrotron. The BCDI detector sits at the end of an arm and has three degrees of freedom, the detector distance and the angles γ, δ, as shown. The origin is located at the center of rotation of the diffractometer within a couple of micrometres. (b) Schematic of the two Bragg peak measurement for the detector calibration. The two $\mathbf{Q}$ vectors correspond to two separate measurements. For the first measurement the crystal is oriented so that the monochromatic beam diffracts from the (111) atomic planes. The intensity of the (111) Bragg peak, which is recorded by the BCDI detector, is optimized by tuning the θ, ϕ, χ angles of the sample stage. Then a Laue pattern is collected at the exact position after switching to the pink beam. The same process is repeated for measuring the (022) Bragg peak and the corresponding Laue pattern at the given position. All coordinate systems are right-handed.

the lattice, the measured diffraction angles can be used to calculate the orientation of the diffracting lattice to an accuracy of 0.01° [80].

When a beam with finite spectral bandwidth illuminates a single crystal, every reciprocal lattice point lying within the shell bounded by the Ewald spheres of the energy bandwidth of the beam will simultaneously be excited. For a 300 nm gold nanocrystal, one may expect four to six reflections on the current Eiger2 500k detector (1024 × 512 pixels, 75 µm × 75 µm pixel size) given the current experimental geometry. In the current experimental configuration, the distance between the detector and focus is around 25 mm. The detector covers a solid angle $\Omega = A/d^2 = 1024 \times 512 \times (75\ \mu\text{m})^2/(25\ \text{mm})^2 \approx 4.7$ sterad.

In a scanning Laue microscopy measurement, a sample containing many crystals is scanned across a broadband beam. For the procedure detailed here, de-wetted gold nanocrystals were grown on a (100) oriented niobium-doped, strontium titanate substrate (0.05 wt% Nb:STO from MSE Supplies). At 34-ID-C, the pink beam energy bandwidth is approximately 5–20 keV (0.8–2.5 Å). The slitted, unfocused X-ray beam is 30 µm × 70 µm. The beam is focused by a set of KB mirrors down to a beam spot of 0.5 µm × 0.7 µm. For the collection of BCDI patterns a Lynx T1 detector with GaAs sensor is used which has a pixel pitch of 55 µm and an orthogonal 512 × 512 grid.

3.2.2 Laue detector calibration

Calibrating the Laue detector geometry is crucial for accuracy and reliability of the determined orientations. For accurately indexing the measured Laue patterns from arbitrarily oriented nanocrystals, it is necessary to determine the detector orientation relative to the laboratory frame to within tens of milliradians or less. Following the implementation used in *LaueGo* the detector is defined by a rotation vector **R** and translation vector **P**, each having three components. Traditionally, the Laue detector calibration at the neighboring 34ID-E endstation consists of two steps. The first step requires recording a Laue pattern from a single-crystal silicon wafer with known crystallographic

orientation and indexing it with *LaueGo* based on estimated **R** and **P** vectors. During the second step, the energy of at least three Laue peaks, seen in the previously recorded Laue pattern, are determined with an accuracy of less than 1 eV by scanning the energy of the X-ray beam. Knowing the energies of the peaks and the lattice constant of silicon, one can determine the orientation of the lattice with high certainty.

At 34-ID-C, the monochromator used for these experiments is not accurate enough to enable this calibration method. Therefore, determining the energy of several peaks with sufficient accuracy is not possible. Additionally, scanning the energy for each of the peaks can be time consuming. However, at 34-ID-C we can determine the 2θ value of a single found monochromatic Bragg peak with high accuracy using the diffractometer. This allows an accurate knowledge of a single X-ray energy and the subsequent determination of the sample orientation when a second Bragg reflection is identified. The procedure can be conducted with a silicon (001) oriented substrate where locating two or more Bragg peaks from the substrate is not difficult. More specifically, the (022) Bragg reflection for silicon is found and the goniometer angles recorded at the position of maximum intensity. This allows the determination of the $\mathbf{Q}_{022}$ diffraction vector simultaneously in the laboratory and crystal frames. By repeating the above steps for a (111) silicon reflection, a second orientation vector is determined in both laboratory and crystal reference frames. The two vectors are depicted in Fig. 3.1(b) and can be expressed in the laboratory and crystal frames through a transformation of axes as

$$\mathbf{Q}_{022}^{\text{cryst}} = \mathbf{g}_{ij} \cdot \mathbf{Q}_{022}^{\text{lab}} \cdot \mathbf{G}_1, \tag{3.1}$$

$$\mathbf{Q}_{111}^{\text{cryst}} = \mathbf{g}_{ij} \cdot \mathbf{Q}_{111}^{\text{lab}} \cdot \mathbf{G}_2, \tag{3.2}$$

$$\theta = \arccos \frac{\mathbf{Q}_{022}^{\text{cryst}} \mathbf{Q}_{111}^{\text{cryst}}}{||\mathbf{Q}_{022}^{\text{cryst}} \mathbf{Q}_{111}^{\text{cryst}}||}, \tag{3.3}$$

where $\mathbf{Q}_{022}^{\text{cryst}}$ is the $\mathbf{Q}_{022}$ diffraction vector in the crystal frame and $\mathbf{Q}_{022}^{\text{lab}}$ is the $\mathbf{Q}_{022}$ diffraction vector in the laboratory frame. Similarly, $\mathbf{Q}_{111}^{\text{cryst}}$ and $\mathbf{Q}_{111}^{\text{lab}}$ are, respectively, the $\mathbf{Q}_{111}$ diffraction vector in the crystal frame and laboratory frame. $\mathbf{g}_{ij}$ is an orientation matrix for the crystal with

respect to the sample reference frame. $\mathbf{G}_i$ is a similar rotation matrix but for the sample with respect to the laboratory frame. Then, orthonormal vector bases are constructed in the laboratory and crystal reference frames and the matrices are derived to transform a vector expressed in the crystal reference frame to the laboratory frame (see Section S1 in the supporting information). Using the known sample orientation and initial guess of **P** and **R** a Laue pattern can be simulated for any arbitrary sample orientation at which a Laue pattern is measured. This is typically done when the sample stage is set to $\theta = 0^\circ$, $\phi = 0^\circ$ and $\chi = 90^\circ$. At these settings, the incident beam is parallel to the surface of the sample. Measurements are taken when the sample is at an angle of incidence of 10°, for the beam to scatter from the sample and diffract to the detector. Note that a pair of the monochromatic beam Bragg peaks are required [e.g. one for the (111) and one for the (022) reflections] and at least one pink beam Laue pattern. Then multivariable optimization algorithms are used to refine the values of the P and R vectors to match the simulated Laue pattern to the measured one (see Section S3 in the supporting information).

The translation vector **P** defines the distance between the center of the detector surface and the origin in the laboratory frame where the beam illuminates the sample, as shown in Fig. 3.1(a). The Rodrigues rotation vector **R** rotates the detector surface from the origin to its actual location. The values of each component of the **P** vector are estimated initially by measuring the horizontal and vertical offsets of the center of the surface of the Laue detector from the origin with a ruler. Each of the aforementioned components of **P** is determined with a couple of millimetres accuracy and formed the initial guess of the translation vector $\mathbf{P} = [0, -25, -65]$ mm. The rotation vector **R** is estimated by determining the rotation matrix and the Rodrigues rotation formula (see Section S3). We assign the initial values of the rotation vector $\mathbf{R} = [2.3, 0.0, 2.2]$ rad, indicating that the detector is placed on the inboard side of the sample facing straight outboard.

The above pair of vectors is optimized by combining the Nelder–Mead algorithm [81] with a grid search method. For the definition of the cost function, the Laue patterns are simulated by the

forward model, compared with the experimental data, and the distances are calculated between the extracted peaks in the experimental data and corresponding nearest peak positions in the forward modeled Laue patterns. We define as loss the mean of the absolute values of distances between predicted and experimentally determined Bragg peaks (see Section S9). The termination criterion for the optimization process is set as a maximum error of less than one pixel. When the optimization reached a value below one pixel the following values for a particular experiment (the values vary each time the apparatus is set up) were obtained for the translation and rotation vectors, respectively, $\mathbf{P} = [-0.653, -25.946, -68.220]$ mm and $\mathbf{R} = [2.23, -0.009, 2.205]$ rad for this work.

Although Nelder–Mead often optimizes the objective function within tens of iterations, it can be trapped in local minima. Accordingly, we varied the initial values for the optimization. More specifically, both **P** and **R** have three independent components. The initial value of P_1 (the first component of **P**) can vary from -5 to 5 mm in steps of 2. Similarly, the initial value of P_2 varies from -20 to -30 mm and P_3 varies from -60 to -70 mm with the same step size as P_1. The initial value of all components in R varies from 0 to 5 rad with a step size of 1 rad. The final values obtained from different initial guesses exhibit variability. Section S9 shows a comparison of the outcomes determined from varying initial values of P_2. We were able to find the optimal value of the components of the translation vector **P** and rotation vector **R** with the same procedure. We conclude that combining Nelder–Mead with a grid search method is effective for this optimization task, which is typically performed once per beam time.

The optimized translation vector **P** and rotation vector **R** are used as input parameters for *LaueGo* to index Laue patterns. The other inputs to *LaueGo* include a list of coordinates of the peak positions on the detector image and the crystal lattice parameters. The lattice parameters of a crystalline material can be determined using techniques such as X-ray diffraction or using standard crystal lattice parameters as reported by Couderc *et al.* [82].

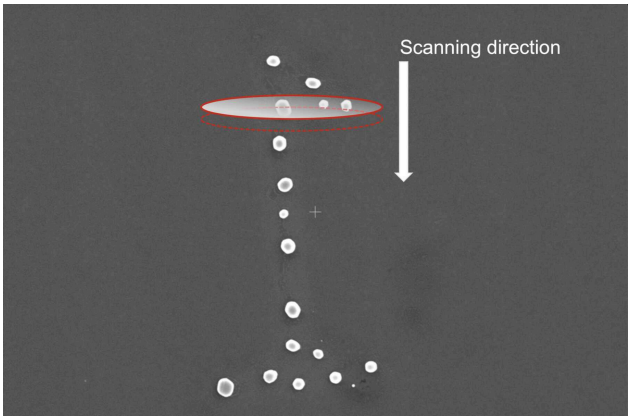

Figure 3.2 Schematic of the scanning for pink beam across a cluster of nanocrystals on the STO substrate. The X-ray beam (approximate footprint shown in red) is impinging on three crystals and moves along the direction of the white arrow. A 2D mesh scan is performed over a total area of 30 μm $\times$ 2 μm using a step size of 250 nm and 500 nm for the vertical and horizontal directions, respectively. This ensures that all nanocrystals in the cluster are illuminated.

3.2.3 Image processing

Figure 3.3 illustrates the overall image processing workflow for scanning Laue diffraction microscopy. The result yields a background-subtracted diffraction pattern with peaks identified from both the substrate and individual nanocrystals. These patterns are then used to calculate a list of orientations and their corresponding spatial positions in the beamline reference frame. For the collection of Laue patterns, the same experimental geometry was used as reported by Pateras *et al.* [59].

We used the pink beam to scan patches of de-wetted, arbitrarily oriented gold nanoparticles on an STO substrate. Each spatial mesh scan was executed using sub-micrometre steps to create redundancy in the data with significant spatial overlap from step to step, shown in Fig. 3.2. At each step in the scan, a Laue image such as the one shown in Fig. 3.3(a)is collected, containing peaks from all nanoparticles illuminated by the beam at that step as well as those from the substrate. Because the sample is at a relatively small incidence angle ($\sim 10^{\circ}$) the beam footprint on the sample

results in greater uncertainty in the position parallel to the direction of elongation.

The next step is to locate the positions of all Laue peaks in the raw data to use for indexing. Several factors complicate image segmentation in these Laue datasets, including the presence of high-intensity substrate peaks, variation in flux across the energy profile of the beam, and diffuse scattering. In particular, the small size of the nanocrystals relative to the substrate makes their peak intensities orders of magnitude lower than the substrate peaks. Furthermore, the energy spectrum of the beam is not uniform, such that reflections fulfilling the Laue criterion at energies with low flux cannot be distinguished from the background.

Background subtraction

The indexing program can only index Laue peaks from one material at a time, so it is necessary to first remove the substrate peaks from every image so that only peaks originating from the nanocrystal remain. Because the substrate is a single-crystal STO wafer, its Laue peaks are practically identical in every image of the mesh scan. Global thresholding does not suffice for segmentation of these high-intensity substrate peaks because non-crystallographic scattering by the nanocrystals on the substrate leads to a strongly varying background. The intensities of some substrate peaks with low flux are on the same scale as the background noise in some regions of the detector.

Because the substrate peaks exist in every detector image, they can be considered as part of the background. This background can be determined by calculating the pixel-wise median value of the intensities over all images. The variation in the number of diffracting nanocrystals from frame to frame creates variability in the background intensity, meaning a datasetwide median background is not sufficient. Nevertheless, this background can be used to locate the substrate peaks. The rolling-ball algorithm (RBA) is used to correct the background before applying a global threshold [83] to segment out the substrate peaks. The RBA can be visualized in the following way. Consider the 2D intensity profile as a 3D surface, where the surface height at each pixel is decided

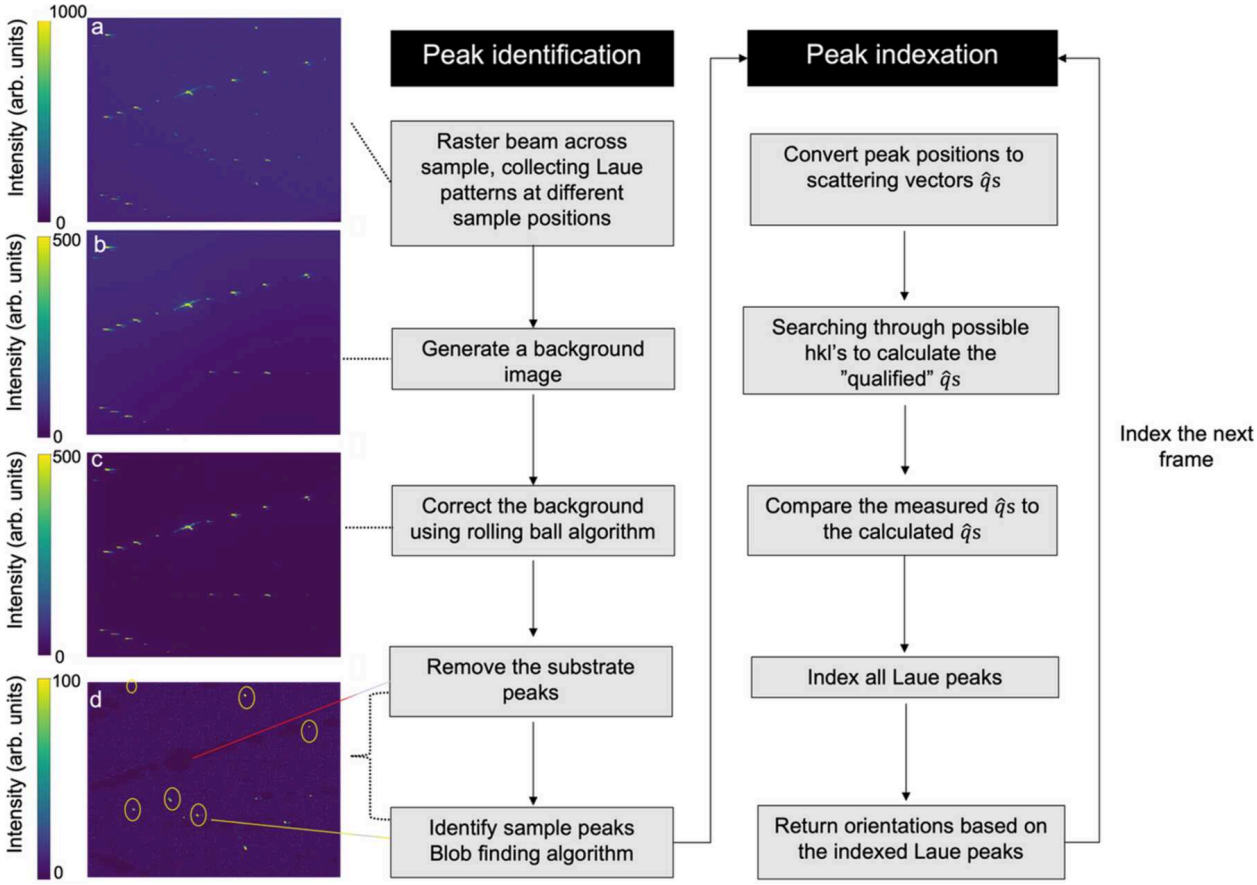

Figure 3.3 Image processing workflow of the scanning Laue diffraction microscopy method including data collection, and automated data analysis. Panel (a) is an example of a diffraction pattern measured on an Au crystal. Panel (b) shows the background calculated from the pixel-wise median value of the intensity. Panel (c) shows the background corrected by applying the rolling ball algorithm to the background. Panel (d) shows the removed substrate peaks denoted by the red line, which correspond to the zero-intensity regions, previously visible as bright peaks in images (a)–(c). In addition, the identified Au peaks are highlighted with a yellow outline.

by its intensity. The RBA determines the background by rolling a sphere of fixed radius across the surface and recording its displacement at every pixel. This displacement surface is the background. Subtracting this surface flattens the background, allowing the peaks to be segmented by a simple global threshold.

Compared with other approaches like local adaptive thresholding [84–86] and automatic thresholding [87–89], the RBA needs only one user input parameter (the radius of the 3D ball) and is computationally efficient [90, 91]. As illustrated in the 1D intensity profile in Fig. 3.4(a), the intensity variation in the raw image is large and the average intensity in the left region of the line profile is much higher than in the right region. For instance, the intensity of a peak (distance $\cong$ 390) is lower than the background in the region near the origin (distance = 0), which makes it indistinguishable from the background using a global threshold. Thus, it is difficult to use simple thresholding to find the peak.

The resulting background (blue solid line) depicts the intensity distribution of the background. The corrected image was generated by subtracting the background obtained from the RBA (blue line) from the raw image (red line). The visibility of the peak seen at $x \cong 390$ has been improved enough so that it can be distinguished much more easily, simplifying the subsequent peak-finding step.

As mentioned, the ball radius is the only algorithmic parameter in RBA but its value depends on the background distribution found in each experimentally acquired image. To reduce the number of manually input parameters, we used the twiddle algorithm in Section S4 [92] to find a radius that minimizes the derivative of the fraction of pixels whose intensities are below a threshold value in the corrected image (raw image with background subtracted) with respect to the tested radius [see Fig. 3.4(b); details can be found in Section S8]. With the background removed, the images are then passed through a global threshold to remove any remaining noise [83]. Using a cluster identification algorithm [93], the location of all intensity clusters (substrate peaks) was identified.

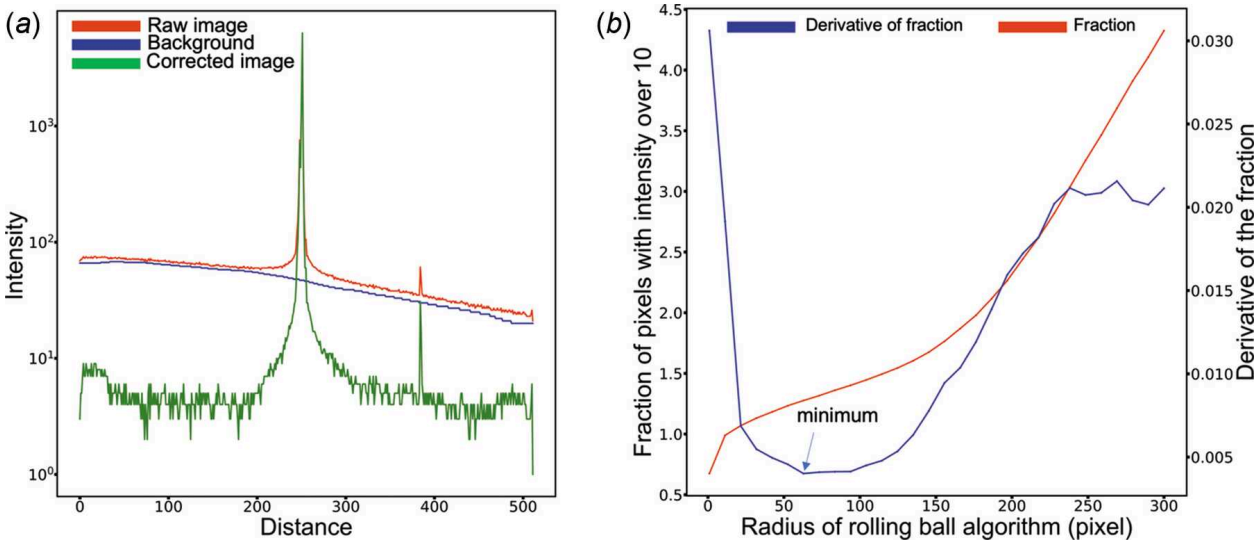

Figure 3.4 (a) Intensity profile of a vertical line of pixels across the detector image [see also Fig. 3.3(a)] before and after using the rolling ball algorithm. The x-axis represents pixels with different distance to the upper pixel of the line on the detector. The y-axis represents the intensity values of the corresponding pixels. The red solid line corresponds to the raw image, the blue solid line corresponds to the resulting background, and the green line corresponds to the corrected image. (b) The fraction of pixels whose intensity is larger than the threshold value and the first derivative of the fraction of pixels with respect to the tested radius (the parameter of the rolling ball algorithm r) plotted as a function of radius.

Nanocrystal peak identification

The next step is to calculate the background and remove the aforementioned intensity clusters from each image in the raw dataset. First, the image is normalized and a Gaussian filter with $\sigma = 20$ is applied to blur the intensities. A median filter is then applied to identify the background for every pixel. Finally, the substrate peaks found in the previous step are subtracted from all raw images. The substrate peaks are enlarged via binary dilation to ensure that intensity fluctuations from frame to frame around each peak are fully removed. Figure 3.5 shows the image before and after the subtraction of bright peaks. The black boxes show where the nanocrystal peaks are.

After background subtraction of the images, the peaks belonging to the nanocrystal sample are extracted from each image. The threshold value for each reduced image is determined by Otsu's approach [87]. This method calculates the histogram for an image and determines a threshold by minimizing intra-class intensity variance. This single intensity threshold separates pixels into two classes—objects and background. The cluster finding tool is used again to locate the peak positions. Though the rolling ball method identifies the vast majority of substrate peaks, there remains a possibility that some dimmer substrate peaks were missed, causing them to be misidentified as nanocrystal peaks. To mitigate this, the orientation of the substrate is used to forward model all potential substrate Laue peaks. Any forward-modeled peaks found within five pixels of a potential substrate peak are then eliminated from the set of nanocrystal peaks.

3.2.4 Indexing

The indexing module is that used in the *LaueGo* package, developed at 34-ID-E [78]. The peak positions on the detector were recorded in millimetres (mm) and are represented by the variable r_l. The center of the detector is the origin $[r_1 = (0,0,0)]$, X pixels increasing along the x direction, Y pixels increasing along the y direction. Using the peak positions r_l on the detector, the detector translation and rotation vectors $\mathbf{P}$ and $\mathbf{R}$ (determined by Laue detector calibration), respectively,

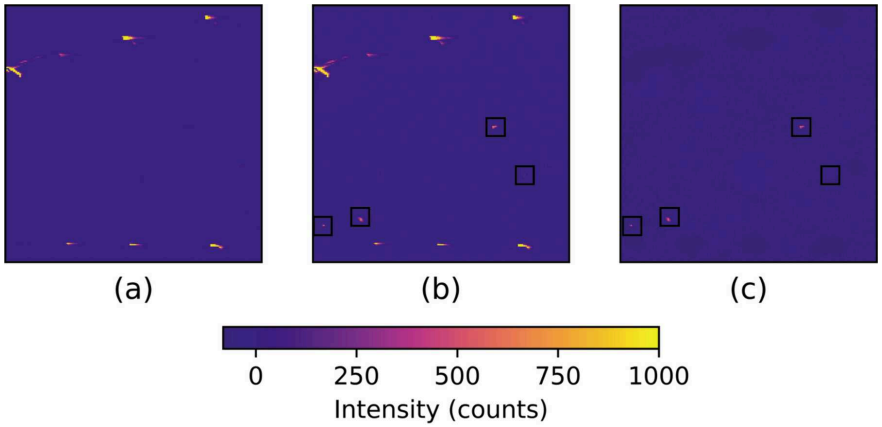

Figure 3.5 (a) A sub-region of the background image [see also Fig. 3.3(c)]. (b) The same sub-region of a raw image before the subtraction of background [see also Fig. 3.3(a)]. (c) The same sub-region of a raw image after the subtraction of background [see also Fig. 3.3(d)].

and the crystallographic lattice parameters of the sample, the unitary scattering vector $\mathbf{g}$ of a Bragg peak is given by $\mathbf{g} = \mathbf{R}(r_l + \mathbf{P})$. The output of the indexing routine is the orientation matrix, whose columns consist of the reciprocal lattice vectors of the crystal. The reciprocal lattice vectors can be directly used to identify and locate all potential Bragg peaks that are accessible to our detector and where BCDI datasets can be measured. The indexing routine is summarized below:

(i) Convert all positions of identified peaks from pixel indices to reciprocal space vectors $\mathbf{q}$ in the laboratory reference frame.

(ii) Use the $\mathbf{q}$ vectors as input for *Euler* (the indexing program in the *LaueGo* package), along with a few threshold values [78]. *Euler* searches through possible $\mathbf{G}_{hkl}$ vectors and calculates the corresponding $\mathbf{q}_s$ (the set of simulated $\mathbf{q}$ vectors by *Euler*). In this process, several threshold values are used to filter out unlikely calculated $\mathbf{q}_s$. First, a maximum energy is chosen to use for searching, which limits how big the $\mathbf{G}_{hkl}$ can get. Second and third is a central $\mathbf{G}_{hkl}$, and cone angle. This allows the user to tell the program approximately where to look for the $\mathbf{G}hkl$ vectors. In our case, the maximum energy for searching is 24 keV, $\mathbf{G}_{001}$ is the central $\mathbf{G}_{hkl}$, and the cone angle is $72^c irc$, which is the maximum needed for cubic crystals.

(iii) Create possible matching pairs based on the measured $\mathbf{q}$ and calculated $\mathbf{q}_s$ and compare angles between two measured $\mathbf{q}$ vectors with the angles between two calculated $\mathbf{q}_s$ vectors. During this process, two threshold values are chosen to determine the possible orientations. The first is a maximum energy to use for matching, which is a larger energy than the maximum energy for searching, that allows the program to identify $\mathbf{G}_{hkl}$ with large energies. In our cases, this energy is 30 keV. The second is an angular tolerance for comparing the angle between two $\mathbf{G}_{hkl}$ vectors with the angle between two $\mathbf{q}$ vectors. In our cases, the angular tolerance is $0.2^c irc$.

(iv) The indexed Laue patterns are used to create a pattern list, which associates each pattern with a location on the sample, orientation matrix, the fitted RMS error of the pattern and the number of matching peaks.

(v) Use the pattern list to calculate the center of mass of each grain. The misorientations between orientations in the pattern list are calculated, then orientations less than an upper limit are considered to be the same grain. Therefore, each grain can include many patterns which appear at different sample-to-beam locations. Finally, the average x and y positions for the grouped grains are calculated and regarded as the center of mass.

After indexing all Laue patterns, a list is generated, which includes all found orientations from gold nanocrystals and the corresponding locations of those crystals on the sample. These orientations are then used to calculate the positions of the Bragg peaks in the laboratory frame of the diffractometer. Then, a set of two orientation vectors are calculated for each grain, the in-plane vector **uvw** and out-of-plane vector **hkl**, which are expressed in 3D-space Cartesian coordinates [59]. Using the in- and out-of-plane vectors, an experiment-management software such as *Spec* [94] is used to calculate all the Bragg peak locations for each indexed crystal, facilitating the multi-peak BCDI dataset collection. The displacement between the pink beam and monochromatic beam on the sample when switching from Laue to BCDI mode is less than 1 mm—see the details of the monochromator design in a paper by Liu *et al.* [95] and our implementation in the paper by Pateras

et al. [59]. To determine the displacement between the monochromatic and pink beam, we used a $CdWO_4$ wafer, which luminesces at the X-ray beam footprint locations.

3.3 Validation

3.3.1 Sample and experimental configuration

The samples consist of de-wetted gold crystals on a (100)-oriented, 0.05 wt% niobium-doped, STO substrate (MSE Supplies). Standard optical lithography was performed with AZ330 photoresist and then developed to provide distinct patches of isolated gold nanocrystals. This facilitated locating specific nanocrystals in EBSD and with the optical microscope at 34-ID-C [96]. Gold was then deposited to 30 nm thickness via thermal evaporation. The final liftoff of the remaining resist was performed in 1-methyl-2-pyrrolidinone (NMP) solution with sonication for 10 min. Afterwards, the sample was rinsed with acetone and deionized water. The sample was then annealed in a furnace at 900 °C for 16 h in air and allowed to cool down slowly to room temperature, similar to methods described elsewhere [97]. The average crystal size is approximately 0.4 μm, making these crystals ideal for BCDI at APS 34-ID-C. Fig. 3.2 shows the lithographically patterned cluster of nanocrystals scanned by the pink beam. The beam size is approximately 0.6 μm $\times$ 0.7 μm; however, the tails of the beam can be tens of micrometres in extent but several orders of magnitude dimmer. The scanned area was roughly 30 μm $\times$ 2 μm. A 2D scan was conducted with step sizes of 500 nm along the x_{lab} (horizontal) direction and 250 nm along the z_{lab} (vertical) direction.

3.3.2 Results and discussion

The automatic indexing method was applied to the experimentally measured data and a grain map was returned, which can be seen in Fig. 3.6. In summary, 19 crystals were indexed from their X-ray Laue patterns. The misorientations of each matching pair between EBSD and Laue

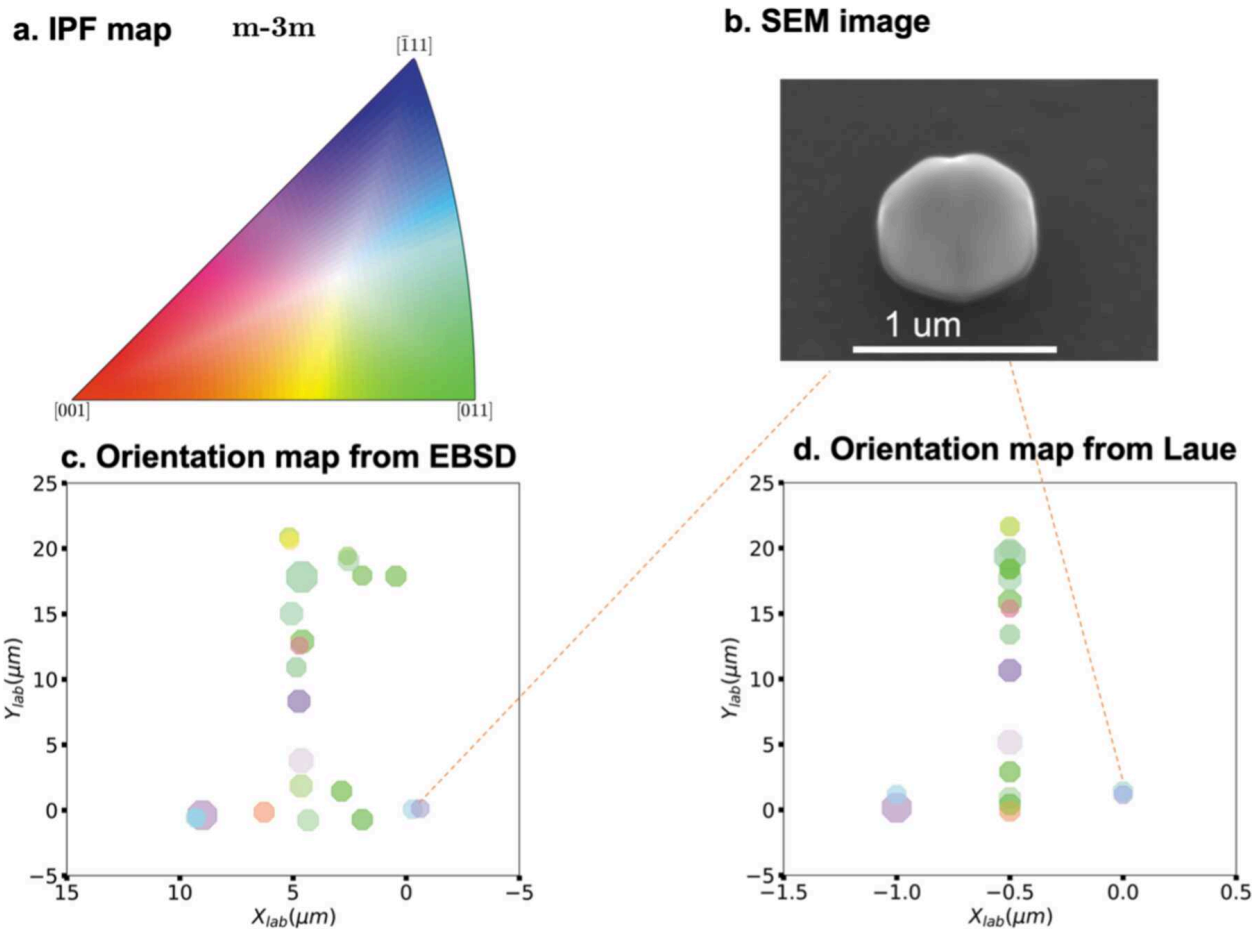

Figure 3.6 (a) An inverse pole figure (IPF) color map for Au. (b) Zoomed image as an example of a twin pair. (c) EBSD map with IPF color representing the orientation of 22 crystals in the transverse direction. (d) Laue map with IPF color representing the orientation of 19 crystal in the transverse direction.

results were calculated and are shown in Table 3.1. From the Laue results, 19 indexed out of 22 nanocrystals are within 19° misorientation to the mean orientation of corresponding crystals in EBSD; 13 nanocrystals are within 10° and 8 nanocrystals are within 6°.

To illustrate the results quantitatively, we conducted a texture analysis from both EBSD and Laue diffraction measurements. According to the pole figures (PFs) from both results shown in Fig. 3.7, the textures are similar to each other in all the PFs. First, nearly all of the crystals have (111) planes normal to the surface of the substrate. Furthermore, we observe an in-plane texture with approximately hexagonal symmetry, likely a consequence of the STO substrate's impact on the preferred alignment of the gold crystals [97]. Figure 3.7 shows that $\{111\}\langle 110\rangle$ texture components exist among the nanocrystals in both experiments indicating that the results from the Laue analysis match well with the EBSD results.

The constructed 2D Laue map shows 19 grains with less than 19° misorientation for cases where the same grain could be identified in EBSD and in Laue. The orientation map obtained from EBSD measurements in Fig. 3.6(c) is compared with the reconstructed 2D orientation map from the Laue indexing result in Fig. 3.6(d). Figure 3.6(c and d) are colored with the inverse pole figure (IPF) color key shown in Fig. 3.6(a) according to the transverse direction in the plane. As a qualitative estimate of the spatial error of our method, we used a scanning electron microscope (SEM) map as the ground truth and calculated the difference between each matched pair from SEM maps and our method. Because we only scanned a length of 2 μm along the z_{lab} direction with a step size of 500 nm, we do not have the spatial resolution to quantify the spatial error in this direction. However, the scan fully covered all the crystals in the cluster within this range. Thus, we chose the large purple grain (crystal ID = 11 in Table 3.1) in the bottom left of Fig. 3.6(c) as the origin and calculated the distance d_i between this grain with each other crystals in the x_{lab} direction, which is the vertical direction in the map. This provided a distance vector $d_{\text{EBSD}} = (d_1, d_2, ..., d_i, ...d_{19})$, where the subscript i is the crystal ID. Meanwhile, we also set the corresponding grain in Fig. 3.6(d)

Crystal ID	Misorientation (°)	Spatial error (μm)	RMS	Peaks indexed	Frames indexed	Bunge Euler angles (ZXZ)
1	16.7	-0.55	0.06	4.6	11	(33.9, 63.8, 130.5)
2	5.19	-0.52	0.02	4.7	6	(93.4, 55.4, 313.6)
3	8.82	-0.87	0.03	5.0	5	(323.8, 50.7, 141.0)
4	5.77	-0.82	0.07	6.0	3	(212.2, 126.8, 130.7)
5	5.59	0.23	0.03	5.0	2	(11.7, 54.5, 138.1)
6	11.83	1.28	0.03	3.0	1	(195.2, 54.8, 312.0)
7	10.78	1.65	0.02	3.8	6	(25.2, 56.8, 135.5)
8	3.94	1.47	0.06	3.7	6	(309.5, 55.8, 188.7)
9	5.88	1.13	0.06	5.7	7	(106.0, 128.3, 316.0)
10	13.79	0.98	0.07	4.0	2	(319.0, 130.4, 144.0)
11	9.16	0.00	0.01	3.6	7	(94.0, 125.5, 133.7)
12	3.14	0.10	0.04	4.8	14	(314.9, 45.9, 194.1)
13	18.64	-0.31	0.04	7.0	1	(203.3, 55.3, 315.2)
14	11.82	-0.26	0.03	5.7	3	(252.7, 143.5, 313.4)
15	8.91	-1.28	0.02	5.0	2	(332.7, 57.0, 228.7)
16	2.57	-0.80	0.02	5.0	5	(126.4, 18.2, 329.7)
17	6.84	0.63	0.08	4.0	2	(23.1, 115.6, 333)
18	5.54	-0.22	0.01	4.5	6	(163.3, 130.0, 195.9)
19	6.17	0.32	0.04	5.1	11	(334.9, 124.3, 135.4)

Table 3.1 Nanocrystals of gold indexed from the Laue diffraction data, along with their misorientation from the corresponding EBSD result.

as the origin and calculated the distance of each other crystal in the x_{lab} direction in the Laue map. The distance vector $d_{\mathrm{Laue}} = (d_1, d_2, ..., d_i, ...d_{19})$ is calculated by the same procedure as for d_{EBSD}. The spatial error is the difference between d_{EBSD} and d_{Laue} and the result is shown in Table 3.1. As mentioned in Section 3.3.1, the tail of the beam is 5 μm. Thus, the absolute value of the spatial error close to or less than 2 μm is precise enough for us to locate the crystals for further BCDI experiments.

There are five reasons for the large misorientations for some grains as well as missing pairs of grains. First, the integrated intensity of the Laue diffraction spots of a given grain is proportional to the illuminated volume of that grain [98]. The grain sizes range from 0.2 to 1.2 μm (see Fig. S4 in Section S5), so the intensity of the Laue reflections varies significantly. Thus, when small nanocrystals are illuminated, planes with low structure factors might not provide enough diffracted intensity, therefore peaks from such crystals are difficult to identify.

Second, error can also arise from nanocrystals rotating and drifting during illumination by high-energy X-rays. Our samples differ from those in the cited paper by Yang *et al.* [73] which are de-wetted Fe–Ni microcrystals on single-crystal sapphire, so their experience with misorientation determination is not necessarily transferable to ours.

The third reason is that the orientation obtained from EBSD is sensitive to (among many other factors) the local surface normal [99]. In a polished polycrystalline sample, this can be assumed to be parallel to the normal to the sample surface, but for the quasi-hemispherical nanocrystals shown in Figs. 3.2 and 3.6(b) there is no guarantee of that. The high-resolution SEM images for crystals (see Fig. S6 in Section S7) show that most crystals are faceted. With such large surface tilts for those highly faceted crystals, it is difficult to index the grains with high confidence using EBSD [99].

The fourth reason is that EBSD mounting can cause the misorientations errors. The mount which was used for both EBSD and the beamline was a simple aluminium SEM stub to which

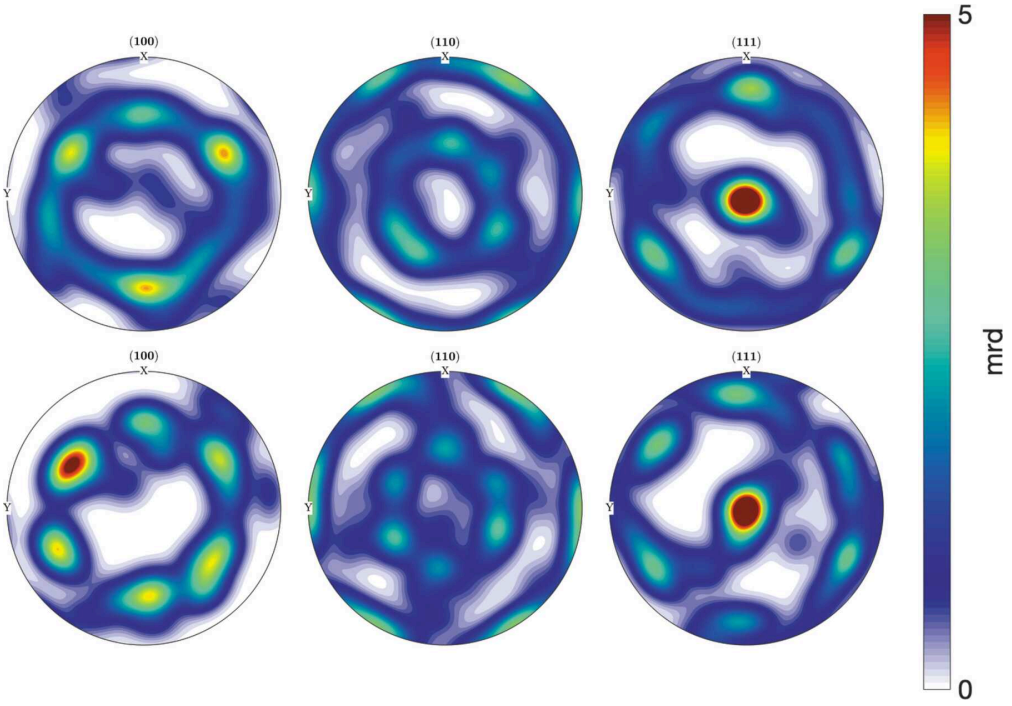

Figure 3.7 Pole figures for the 22 gold nanocrystals from EBSD experiment (top) and 19 Laue results (bottom).

the sample was attached with double-sided carbon tape. The tilt angle used in EBSD analysis is nominally 70°, but we did not calibrate this angle for the measurement. The net result is that there can easily be a few degrees offset between the orientation reported by the EBSD measurement and the true orientation. Therefore, less than 19° of misorientation is acceptable when we qualitatively match our Laue index results with EBSD results.

The last reason is the inability of *LaueGo* to reliably index overlapping Laue patterns. For example, when more than four grains are illuminated and there are five or fewer identified peaks for each grain, *LaueGo* is likely to return only a subset of correct orientations and/or the false-positive orientations. However, *LaueGo* does provide the output orientation for each grain along with the corresponding RMS error and the number of matched peaks from the experimental data and forward-modeled data. We explored the RMS error and the number of matched peaks for each orientation. The results from the correctly indexed crystals are shown in Table 3.1. The highest RMS

error is 0.08, which is smaller than those of most false-positive orientations (RMS error $\leq$ 0.2). The number of matched peaks is another good indicator of the reliability of the experimentally obtained orientations. When the number of peaks is equal to or greater than four, it is highly likely that the indexing is correct. The fractional value is because the crystal is found among different frames and the average of peaks for the same crystal are calculated. If the same crystal appears more than once in the continuous frames or spatially equivalent frames, the orientation is highly likely to be correct. For example, *LaueGo* only indexed three peaks, using one or a few useful parameters for determining the 'goodness' of the orientation result. The RMS error, the average number of indexed peaks, and the number of indexed frames for the matching crystals are shown in Table 3.1.

In our approach, the Laue diffraction is likely to be more precise for orientation determination at 34-ID-C than EBSD. This is also evident in the work of Yang *et al.* [73] who found that the average angular mismatch between orientation matrices misorientations between the Laue and BCDI is 4°, and that between EBSD and BCDI is 6°. We developed our own Laue diffraction technique which is intended to improve upon that available to Yang *et al.* [73]. For instance, we improved the detector calibration step (see Section 3.2.2) and increased the accuracy of the detector positioning parameters, which results in the better accuracy of the indexing results. Despite EBSD measurement being widely accepted in the materials community, it is not necessarily the ground truth for isolated crystals with curved surfaces, as we discuss above.

To validate the accuracy of the Laue measurements we successfully moved the Bragg detector to the calculated positions of certain Bragg peaks from the twin crystals and measured them. The misalignment observed between the orientation determined by Laue diffraction analysis and the actual orientation at which the monochromatic Bragg reflection was found to be less than 0.1°. Thus, we concluded that the micro-Laue diffraction is more accurate compared with EBSD to orient nanocrystals at 34-ID-C, which matches the report by Yang *et al.* [73]. In order to illustrate the randomness of the misorientations, we show multiple examples of combined PFs of different

crystals from EBSD and Laue (see Section S10) and find that the discrepancy of orientations (misorientations) from the two analyses lacks any systematic pattern, i.e. there is no systematic offset between the Laue and EBSD measurements of orientation.

Knowing the orientations and corresponding grain locations, the in- and out-of-plane vectors **uvw** and **hkl** [59] for each grain are calculated. These two vectors are then inserted into Spec and the diffractometer is moved to the correct orientation for a desired Bragg peak. The orientations and corresponding grain locations can be used for identifying twin crystals. First, face-centred-cubic Σ3 twin boundaries can be described as a 60° rotation about a (111) crystal axis. Second, the precision of the twin orientation relationship means that a pair of twin-related crystals must be neighboring grains, so the distance between them should be small. All this means that a twin boundary is convenient as a highly precise boundary type that serves as a marker of a pair of adjacent grains. In this particular cluster, we collected multiple peaks from one pair of twinned crystals in a single grain. The reconstruction of this dataset is beyond the scope of this paper.

3.4 Conclusions

We present a workflow for automatic indexing of sets of isolated nanocrystals at the 34-ID-C endstation of the Advanced Photon Source that generates a spatial orientation map that is intended to facilitate subsequent measurement of BCDI datasets. We indexed 19 out of 22 nanocrystals within 19° misorientation to the mean orientation of corresponding crystals in EBSD—13 nanocrystals are within 10° and 8 are within 6°. Previously, acquiring the orientation for each crystal required manual peak identification and indexing, which takes several hours for data collection and data analysis by hand. We acquired the data and indexed the orientations for a set of isolated nanocrystals within 10 min using our method. The ability to index orientations from isolated crystals is expected to generalize to polycrystalline materials.

Chapter 4

Next Steps

The work presented in this thesis represents an important contribution to Bragg coherent diffraction imaging (BCDI) as well as to the broader field of materials science. Unfortunately, it has not yet accomplished its original purpose: the time-resolved observation of an interaction between a dislocation and a grain boundary. Furthermore, there are other areas for expansion that can aide in this endeavour, both in the short-term, such as the implementation multigrain reconstruction methods, and in the long term such as educational opportunities to build the workforce of the future. In this chapter, I discuss these efforts as part of a proposed doctoral research plan.

4.1 Mesoscale strain dynamics

Existing BCDI reconstruction methods have already demonstrated the ability to image mesoscale strain. The challenge now is creating an experiment that can induce a dislocation and image it multiple times as it moves through the material. The cross-sectional area and coherence length of a synchrotron beam, along with the Bragg condition itself, all impose strict constraints on the imaging window. Even with automated realignment software, the crystal must remain translationally stable to within hundreds of nanometers and rotationally stable to within a few tenths of a degree

for each measurement. Greater than this, however, is the task of making sure that the dislocation itself remains stable throughout a single measurement, a process which has hitherto involved hours of exposure interspersed with multiple reorientations of the crystal to capture different peaks. Fortunately, the ongoing upgrade to the APS will alleviate one of those factors, as the dramatically increased coherent flux will result in a proportional decrease in exposure time.

On multiple occasions, we have tried to introduce dislocations by using an atomic force microscope (AFM) to make nano-indentations on gold crystals. However, the AFM's limited precision, instability while mounted, and sensitivity to vibration and radiation pressure have prevented us from achieving the desired temporal resolution. Radiation pressure is particularly problematic when considering the APS upgrade. Additionally, placing the AFM tip in contact with the sample also places it in the X-ray beam, which produces noise in the diffraction pattern and reduces spatial resolution. Because of these factors, I am doubtful that AFM indentation is capable of producing sufficiently stable dislocations for dynamic imaging.

Heating is, in my opinion, a more promising approach. When the system is heated, the interface between sample and substrate could become a source of strain based on a difference in thermal expansion. Assuming that a difference in expansion equivalent to one lattice unit a will produce two dislocations (the sample-substrate contact is 2-dimensional), we could estimate the change in temperature ΔT required to produce N dislocations as

$$\Delta T = \frac{Na}{2l(\Delta\sigma)}, \tag{4.1}$$

where l is the length of the linear size of the crystal and $\Delta\sigma$ is the difference in thermal expansion coefficients between the sample and substrate. The samples used in Chapters 2 and 3 consist of Au crystals ($a = 0.4078$ nm, $l \approx 0.75$ μm) on a $SrTiO_3$ substrate, which leads to a $\Delta\sigma$ of 4.8×10^{-6} K^{-1}. Based on these values, we can expect the interface to form a dislocation after a temperature change of 56 K.

This would be more stable for a number of reasons. First, it requires temperature control on the

order of tens of kelvin rather than the more difficult positional control on the order of nanometers. Second, it involves no moving parts, which makes it much easier to maintain that control while reorienting the sample. Finally, it allows the sample to remain isolated, which reduces the amount of noise in the diffraction pattern. I am eager to investigate using thermal expansion as a means of inducing atomic dislocations.

4.2 Multi-grain reconstruction

Building on the success of coupled phase retrieval methods, we can also consider placing further constraints by coupling the reconstructions of two or more adjacent grains. Some work has already been done in this area by Matthew Wilkin [100]. He showed that periodic alignment of the two grains and mutual exclusion of overlapping support regions can be an effective constraint on a joint reconstruction. Twin grains are particularly straightforward to align due to their planar boundary. By correlating the gradient of the two objects perpendicular to that interface, he was able to quite effectively align reconstructions in a shared direct space. There is still a significant amount of work to be done in order to apply this method to arbitrary grain boundaries.

This method is conceptually quite similar to his multipeak CPR method which I briefly describe in Chapter 2 as periodic-constrained optimization (PCO). While the multigrain processes are computationally separate from the multipeak processes and therefore his scheme could be implemented with my own algorithm, the periodic nature of his multigrain method has led me to question whether there may also be a cyclic/serial approach to this problem. This is something I would like to investigate further.

4.3 Error metrics in iterative phase retrieval

One of the most common methods of iterative phase retrieval consists of alternating blocks of hybrid input-output (HIO) and error reduction (ER). Unlike most optimization algorithms, the HIO/ER technique notably lacks an algorithmic stopping criterion. Nominally, the ER update function should minimize the chi-square error between the reconstructed and measured diffraction amplitudes [17]. However, this metric has been shown to be quite ineffective at distinguishing between real and false solutions due to the ubiquity of local minima, particularly in the presence of noise [101]. This, combined with the effectiveness of the HIO algorithm at avoiding stagnation, has encouraged an approach to phase retrieval based on "recipes" (fixed sequence of iterations). If a recipe doesn't work, the immediate response is often just to make it longer.

While developing my CCO approach, I examined many different error metrics and found that most of them had the same problem as chi-square (see Section 2.6.2). However, I also discovered a new metric, hitherto unpublished to my knowledge, which I refer to as the expected histogram deviation (EHD). This metric is unique among those I have tested in that it exhibits a fundamental change in its behavior during the reconstruction process. This phase-transition-like phenomenon could make it possible to use the EHD metric as a stopping criterion for iterative phase retrieval. If I continue in a doctoral program, I will look into how this could be used to push toward a recipe-independent phase retrieval routine.

4.4 Educational opportunities

Like most advanced fields, coherent diffraction imaging can be difficult for a novice to break into, as there are few resources dedicated to easing the learning curve. As a TA in the physics 245 lab class, I was involved in some efforts to change this. The portion of that class dedicated to lasers and optics utilizes nearly all of the important components involved in basic CDI. I helped develop

a curriculum which shifts the focus of this part of the class onto image processing and CDI. This allows students the opportunity to develop a basic understanding of CDI principles without having to join a specific research group. Additionally, I have written some software (see Section A.3) designed to build understanding of how phase retrieval algorithms work.

Unlike other points discussed in this chapter, much of the work here has already been accomplished. I am currently in the process of writing a journal article titled "Principles of advanced imaging in an undergraduate laboratory," with plans to submit the manuscript to *The American Journal of Physics*. I also plan to continue development of the Interactive-CDI software.

4.5 Doctoral research plan

While the APS upgrade means that, in the near-term, it will be difficult to collect the data necessary to observe mesoscopic strain dynamics, the downtime affords a valuable opportunity to further develop existing reconstruction methods. This would include an implementation of Wilkin's multigrain algorithm, an implementation of an EHD-based stopping criterion, and experimentation with serial multigrain reconstruction methods. Additionally, I have been involved in several other projects, such as investigating the robustness of Au/STO samples against radiation pressure, developing the phase retrieval software *Cohere*, and examining the impact of resampling BCDI data into a common grid. As shown in Table 4.1, this puts me in a position with the potential to produce five first-author papers and three co-author papers over the next few years.

Year	Semester	Role	Tentative title
2024	Winter	Author	Principles of advanced imaging in an undergraduate laboratory
2024	Summer	Co-author	Properties of Au microcrystals on a $SrTiO_3$ substrate
2024	Summer	Co-author	Joint reconstruction of twin-grain Au bicrystal using shared Bragg peak
2024	Fall	Author	Expected histogram deviation as a stopping criterion for multi-peak Bragg coherent diffraction imaging
2024	Fall	Co-author	Cohere: Bragg coherent diffraction imaging software for single- and multipeak reconstructions
2025	Winter	Author	Effects of resampling on reconstruction fidelity in Bragg coherent diffraction imaging
2025	Fall	Author	Time-resolved imaging of interaction between dislocations and grain boundaries
2026	Winter	Author	Ph.D. Dissertation

Table 4.1 Prospective list of publications which I hope to author/co-author during my time as a Ph.D. student.

Chapter 5

Conclusion

The research described in this thesis, both completed and yet to be done, has the potential to deepen our understanding of how material strain affects materials performance and lifetime. The implementation of CCO multipeak phase retrieval into Cohere makes it possible to analyze multipeak data at a rate that can keep up with the data production rates of next-generation coherent X-ray sources, such as the APS-U. The development of Laue diffraction based orientation mapping methods makes it much easier to do in situ experimentation on microcrystals and may even be extensible to bulk polycrystals. Both of these are important for steps towards the development of a standard workflow for studying mesoscopic strain dynamics.

Appendix A

Software

Though not a primary focus of the papers included in Chapters 2 and 3, a substantial portion of my research has consisted of developing software. The following sections briefly introduce some software projects I have worked on in conjunction with the research presented in this thesis.

A.1 Cohere

The article in Chapter 2 briefly mentions Cohere as the primary reconstruction software for the 34-ID-C beamline at the Advanced Photon Source (APS). This Python-based software was primarily developed by Barbara Frosik and Ross Harder for single-peak reconstructions. I was the primary developer for Cohere's multipeak capabilities. The cyclic-constrained optimization (CCO) approach to multipeak phase retrieval involves many processes also used in single-peak reconstructions. This, combined with Cohere's highly object-oriented source code, made it possible for the multipeak reconstruction features to inherit many processes from existing code. Such inheritance helps to ensure that the continued development of Cohere's core processes will not lead to future compatibility issues between the single- and multipeak functionality.

The source code for Cohere is publicly available on Github at AdvancedPhotonSource/cohere

and AdvancedPhotonSource/cohere-ui. Additionally, a publication is currently in development which will describe the software and make it citeable.

A.2 Lauepy

The method of scanning Laue orientation mapping described in Chapter 3 was developed primarily by Matt Wilkin and Yueheng Zhang. I developed their original Python scripts into a more organized and streamlined package, which I called Lauepy. The purpose of this was simply to make a disorganized workflow more user-friendly, particularly for those unfamiliar with the original research involved in its development. A key feature of this was the implementation of a graphical interface, which removes a significant barrier for any user unfamiliar with Python. In addition, the image processing in Lauepy is significantly faster and more effective than what was published in the paper due to a highly efficient approximation of the rolling ball algorithm (see Section 3.2.3), which allows for the application of multiple filters of different radii.

The source code for Lauepy is publicly available on Github at jacione/lauepy, and has a citeable DOI [61] through Zenodo.

A.3 Interactive-CDI

Interactive-CDI is a phase retrieval software with the the stated goal of "transparency rather than efficiency." It allows a user to progress step-by-step through some common phase retrieval algorithms [17, 25, 26, 58] while observing the reconstruction in real time. The image used for phase retrieval may be simulated or real, color or monochrome, and most image file types are supported. This software is now being used in the advanced undergraduate physics lab class (Physics 245) at BYU, where students have reconstructed complicated multi-pinhole apertures from measured diffraction intensities.

The source code for Interactive-CDI (as well as a compiled application for Windows) is publicly available on Github at jacione/interactive-cdi. It also has a citeable DOI [102] through Zenodo.

Bibliography

[1] E. van der Giessen *et al.*, "Roadmap on Multiscale Materials Modeling," Modelling Simul. Mater. Sci. Eng. **28,** 043001 (2020).

[2] W. S. Slaughter, *The Linearized Theory of Elasticity* (Birkhäuser Boston, Boston, MA, 2002).

[3] C. Kittel, *Introduction to Solid State Physics*, global edition, [9th edition] ed. (Wiley, Hoboken, NJ, 2018).

[4] R. J. Asaro, "Micromechanics of Crystals and Polycrystals," in *Advances in Applied Mechanics*, J. W. Hutchinson and T. Y. Wu, eds., (Elsevier, 1983), Vol. 23, pp. 1–115.

[5] T. W. Clyne and J. E. Campbell, *Testing of the Plastic Deformation of Metals*, 1 ed. (Cambridge University Press, 2021).

[6] M. Ware and J. Peatross, *Physics of Light and Optics* (2015).

[7] E. Ortega, D. Nicholls, N. D. Browning, and N. de Jonge, "High Temporal-Resolution Scanning Transmission Electron Microscopy Using Sparse-Serpentine Scan Pathways," Sci Rep **11,** 22722 (2021).

[8] J. Jung *et al.*, "Scaling Molecular Dynamics beyond 100,000 Processor Cores for Large-Scale Biophysical Simulations," Journal of Computational Chemistry **40,** 1919–1930 (2019).

[9] G. Crabtree *et al.*, "From Quanta to the Continuum: Opportunities for Mesoscale Science," Technical report, USDOE Office of Science (SC) (United States) (2012) .

[10] W. Röntgen, "On a New Kind of Rays," Nature **53,** 274–276 (1896).

[11] G. J. Williams, M. A. Pfeifer, I. A. Vartanyants, and I. K. Robinson, "Three-Dimensional Imaging of Microstructure in Au Nanocrystals," Phys. Rev. Lett. **90,** 175501 (2003).

[12] M. A. Pfeifer, Ph.D. thesis, University of Illlinois at Urbana-Champaign, 2005.

[13] H. N. Chapman *et al.*, "High-Resolution Ab Initio Three-Dimensional x-Ray Diffraction Microscopy," J. Opt. Soc. Am. A, JOSAA **23,** 1179–1200 (2006).

[14] M. A. Pfeifer, G. J. Williams, I. A. Vartanyants, R. Harder, and I. K. Robinson, "Three-Dimensional Mapping of a Deformation Field inside a Nanocrystal," Nature **442,** 63–66 (2006).

[15] I. Robinson and R. Harder, "Coherent X-ray Diffraction Imaging of Strain at the Nanoscale," Nature Mater **8,** 291–298 (2009).

[16] H. N. Chapman and K. A. Nugent, "Coherent Lensless X-ray Imaging," Nature Photon **4,** 833–839 (2010).

[17] J. R. Fienup, "Phase Retrieval Algorithms: A Comparison," Appl. Opt., AO **21,** 2758–2769 (1982).

[18] W. H. Bragg and W. L. Bragg, "The Reflection of X-rays by Crystals," Proceedings of the Royal Society of London. Series A, Containing Papers of a Mathematical and Physical Character **88,** 428–438 (1913).

[19] P. P. Ewald, "Introduction to the Dynamical Theory of X-ray Diffraction," Acta Cryst A **25,** 103–108 (1969).

[20] D. Francom *et al.*, "Simulation and Emulation of X-Ray Diffraction from Dynamic Compression Experiments," J. dynamic behavior mater. **7,** 170–187 (2021).

[21] D. Sayre, "Prospects for Long-Wavelength X-ray Microscopy and Diffraction," in *Imaging Processes and Coherence in Physics*, M. Schlenker, M. Fink, J. P. Goedgebuer, C. Malgrange, J. Ch. Vieénot, and R. H. Wade, eds., (Springer Berlin Heidelberg, Berlin, Heidelberg, 1980), Vol. 112, pp. 229–235.

[22] J. W. Goodman, *Introduction to Fourier Optics* (Roberts & Company Publishers, 2005).

[23] R. E. Burge, M. A. Fiddy, A. H. Greenaway, and G. Ross, "The Phase Problem," Proc R Soc London Ser A **350,** 191–212 (1976).

[24] J. R. Fienup, "Reconstruction of an Object from the Modulus of Its Fourier Transform," Opt. Lett., OL **3,** 27–29 (1978).

[25] J. R. Fienup, "Reconstruction of a Complex-Valued Object from the Modulus of Its Fourier Transform Using a Support Constraint," J. Opt. Soc. Am. A, JOSAA **4,** 118–123 (1987).

[26] S. Marchesini, H. He, H. N. Chapman, S. P. Hau-Riege, A. Noy, M. R. Howells, U. Weierstall, and J. C. H. Spence, "X-Ray Image Reconstruction from a Diffraction Pattern Alone," Phys. Rev. B **68,** 140101 (2003).

[27] F. Hofmann, E. Tarleton, R. J. Harder, N. W. Phillips, P.-W. Ma, J. N. Clark, I. K. Robinson, B. Abbey, W. Liu, and C. E. Beck, "3D Lattice Distortions and Defect Structures in Ion-Implanted Nano-Crystals," Sci Rep **7,** 45993 (2017).

[28] M. C. Newton, "Concurrent Phase Retrieval for Imaging Strain in Nanocrystals," Phys. Rev. B **102,** 014104 (2020).

[29] Y. Gao, X. Huang, H. Yan, and G. J. Williams, "Bragg Coherent Diffraction Imaging by Simultaneous Reconstruction of Multiple Diffraction Peaks," Phys. Rev. B **103,** 014102 (2021).

[30] M. J. Wilkin, S. Maddali, S. O. Hruszkewycz, A. Pateras, R. L. Sandberg, R. Harder, W. Cha, R. M. Suter, and A. D. Rollett, "Experimental Demonstration of Coupled Multi-Peak Bragg Coherent Diffraction Imaging with Genetic Algorithms," Phys. Rev. B **103,** 214103 (2021).

[31] S. Maddali *et al.*, "Concurrent Multi-Peak Bragg Coherent x-Ray Diffraction Imaging of 3D Nanocrystal Lattice Displacement via Global Optimization," npj Comput Mater **9,** 1–12 (2023).

[32] A. L. Patterson, "The Diffraction of X-Rays by Small Crystalline Particles," Phys. Rev. **56,** 972–977 (1939).

[33] R. Harder, M. A. Pfeifer, G. J. Williams, I. A. Vartaniants, and I. K. Robinson, "Orientation Variation of Surface Strain," Phys. Rev. B **76,** 115425 (2007).

[34] V. Favre-Nicolin *et al.*, "Analysis of Strain and Stacking Faults in Single Nanowires Using Bragg Coherent Diffraction Imaging," New J. Phys. **12,** 035013 (2010).

[35] M. C. Newton, S. J. Leake, R. Harder, and I. K. Robinson, "Three-Dimensional Imaging of Strain in a Single ZnO Nanorod," Nature Mater **9,** 120–124 (2010).

[36] W. Yang, X. Huang, R. Harder, J. N. Clark, I. K. Robinson, and H.-k. Mao, "Coherent Diffraction Imaging of Nanoscale Strain Evolution in a Single Crystal under High Pressure," Nat Commun **4,** 1680 (2013).

[37] A. Ulvestad *et al.*, "In Situ 3D Imaging of Catalysis Induced Strain in Gold Nanoparticles," J. Phys. Chem. Lett. **7,** 3008–3013 (2016).

[38] A. Ulvestad *et al.*, "Three-Dimensional Imaging of Dislocation Dynamics during the Hydriding Phase Transformation," Nature Mater **16,** 565–571 (2017).

[39] A. Yau, W. Cha, M. W. Kanan, G. B. Stephenson, and A. Ulvestad, "Bragg Coherent Diffractive Imaging of Single-Grain Defect Dynamics in Polycrystalline Films," Science **356,** 739–742 (2017).

[40] M. J. Cherukara, R. Pokharel, T. S. O'Leary, J. K. Baldwin, E. Maxey, W. Cha, J. Maser, R. J. Harder, S. J. Fensin, and R. L. Sandberg, "Three-Dimensional X-ray Diffraction Imaging of Dislocations in Polycrystalline Metals under Tensile Loading," Nat Commun **9,** 3776 (2018).

[41] S. O. Hruszkewycz, S. Maddali, C. P. Anderson, W. Cha, K. C. Miao, M. J. Highland, A. Ulvestad, D. D. Awschalom, and F. J. Heremans, "Strain Annealing of SiC Nanoparticles Revealed through Bragg Coherent Diffraction Imaging for Quantum Technologies," Phys. Rev. Mater. **2,** 086001 (2018).

[42] A. Singer *et al.*, "Nucleation of Dislocations and Their Dynamics in Layered Oxide Cathode Materials during Battery Charging," Nat Energy **3,** 641–647 (2018).

[43] T. Kawaguchi *et al.*, "Gas-Induced Segregation in Pt-Rh Alloy Nanoparticles Observed by In Situ Bragg Coherent Diffraction Imaging," Phys. Rev. Lett. **123,** 246001 (2019).

[44] F. Hofmann, N. W. Phillips, S. Das, P. Karamched, G. M. Hughes, J. O. Douglas, W. Cha, and W. Liu, "Nanoscale Imaging of the Full Strain Tensor of Specific Dislocations Extracted from a Bulk Sample," Phys. Rev. Materials **4,** 013801 (2020).

[45] M. Eriksson, J. F. van der Veen, and C. Quitmann, "Diffraction-Limited Storage Rings – a Window to the Science of Tomorrow," J Synchrotron Rad **21,** 837–842 (2014).

[46] E. Weckert, "The Potential of Future Light Sources to Explore the Structure and Function of Matter," IUCrJ **2,** 230–245 (2015).

[47] M. Yabashi and H. Tanaka, "The next Ten Years of X-ray Science," Nature Photon **11,** 12–14 (2017).

[48] J. R. R. A. Martins and A. Ning, *Engineering Design Optimization*, 1 ed. (Cambridge University Press, 2021).

[49] J. M. Rodenburg and H. M. L. Faulkner, "A Phase Retrieval Algorithm for Shifting Illumination," Applied Physics Letters **85,** 4795–4797 (2004).

[50] A. M. Maiden and J. M. Rodenburg, "An Improved Ptychographical Phase Retrieval Algorithm for Diffractive Imaging," Ultramicroscopy **109,** 1256–1262 (2009).

[51] A. Maiden, D. Johnson, and P. Li, "Further Improvements to the Ptychographical Iterative Engine," Optica **4,** 736 (2017).

[52] S. Kandel, S. Maddali, Y. S. G. Nashed, S. O. Hruszkewycz, C. Jacobsen, and M. Allain, "Efficient Ptychographic Phase Retrieval via a Matrix-Free Levenberg-Marquardt Algorithm," Opt. Express, OE **29,** 23019–23055 (2021).

[53] S. Maddali *et al.*, "General Approaches for Shear-Correcting Coordinate Transformations in Bragg Coherent Diffraction Imaging. Part I," J Appl Cryst **53,** 393–403 (2020).

[54] W. Burger and M. J. Burge, *Principles of Digital Image Processing: Core Algorithms*, *Undergraduate Topics in Computer Science* (Springer London, London, 2009).

[55] C. Shannon, "Communication in the Presence of Noise," Proceedings of the IRE **37,** 10–21 (1949).

[56] D. Sayre, "Some Implications of a Theorem Due to Shannon," Acta Cryst **5,** 843–843 (1952).

[57] J. Miao and D. Sayre, "On Possible Extensions of X-ray Crystallography through Diffraction-Pattern Oversampling," Acta Cryst A **56,** 596–605 (2000).

[58] R. W. Gerchberg and W. O. Saxton, "A Practical Algorithm for the Determination of Phase from Image and Diffraction Plane Pictures," Optik 35 (1972).

[59] A. Pateras *et al.*, "Combining Laue Diffraction with Bragg Coherent Diffraction Imaging at 34-ID-C," J Synchrotron Rad **27,** 1430–1437 (2020).

[60] Y. Zhang *et al.*, "Mapping Nanocrystal Orientations via Scanning Laue Diffraction Microscopy for Multi-Peak Bragg Coherent Diffraction Imaging," J Synchrotron Rad **30,** 796–806 (2023).

[61] N. Porter, "Lauepy,", Zenodo, 2023.

[62] D. Shapiro *et al.*, "Biological Imaging by Soft X-Ray Diffraction Microscopy," Proceedings of the National Academy of Sciences **102,** 15343–15346 (2005).

[63] Z. Wang, A. Bovik, H. Sheikh, and E. Simoncelli, "Image Quality Assessment: From Error Visibility to Structural Similarity," IEEE Transactions on Image Processing **13,** 600–612 (2004).

[64] F. Maes, A. Collignon, D. Vandermeulen, G. Marchal, and P. Suetens, "Multimodality Image Registration by Maximization of Mutual Information," IEEE Transactions on Medical Imaging **16,** 187–198 (1997).

[65] C. Studholme, D. L. G. Hill, and D. J. Hawkes, "An Overlap Invariant Entropy Measure of 3D Medical Image Alignment," Pattern Recognition **32,** 71–86 (1999).

[66] M. Feixas, A. Bardera, J. Rigan, Q. Xu, and M. Sbert, *Information Theory Tools for Image Processing*, *Synthesis Lectures on Computer Graphics and Animation* (Springer International Publishing, Cham, 2014).

[67] S. J. L. Billinge and I. Levin, "The Problem with Determining Atomic Structure at the Nanoscale," Science **316,** 561–565 (2007).

[68] M. A. Meyers and K. K. Chawla, *Mechanical Behavior of Materials*, 2 ed. (Cambridge University Press, Cambridge, 2008).

[69] M. Bechthold and J. C. Weaver, "Materials Science and Architecture," Nat Rev Mater **2,** 1–19 (2017).

[70] A. Ulvestad, A. Singer, J. N. Clark, H. M. Cho, J. W. Kim, R. Harder, J. Maser, Y. S. Meng, and O. G. Shpyrko, "Topological Defect Dynamics in Operando Battery Nanoparticles," Science **348,** 1344–1347 (2015).

[71] I. K. Robinson, I. A. Vartanyants, G. J. Williams, M. A. Pfeifer, and J. A. Pitney, "Reconstruction of the Shapes of Gold Nanocrystals Using Coherent X-Ray Diffraction," Phys. Rev. Lett. **87,** 195505 (2001).

[72] F. Hofmann, N. W. Phillips, R. J. Harder, W. Liu, J. N. Clark, I. K. Robinson, and B. Abbey, "Micro-Beam Laue Alignment of Multi-Reflection Bragg Coherent Diffraction Imaging Measurements," J Synchrotron Rad **24,** 1048–1055 (2017).

[73] D. Yang *et al.*, "Refinements for Bragg Coherent X-ray Diffraction Imaging: Electron Backscatter Diffraction Alignment and Strain Field Computation," J Appl Cryst **55,** 1184–1195 (2022).

[74] A. B. Greilinger, "A Back-Reflection Laue Method for Determining Crystal Orientation," Zeitschrift für Kristallographie - Crystalline Materials **91,** 424–432 (1935).

[75] X. R. Huang, "LauePt, a Graphical-User-Interface Program for Simulating and Analyzing White-Beam X-ray Diffraction Laue Patterns," J Appl Cryst **43,** 926–928 (2010).

[76] *Strain and Dislocation Gradients from Diffraction: Spatially-Resolved Local Structure and Defects*, R. Barabash and G. Ice, eds., (Imperial College Press, London, 2014).

[77] D. Ferreira Sanchez, J. Villanova, J. Laurencin, J.-S. Micha, A. Montani, P. Gergaud, and P. Bleuet, "X-Ray Micro Laue Diffraction Tomography Analysis of a Solid Oxide Fuel Cell," J Appl Cryst **48,** 357–364 (2015).

[78] W. Liu, G. E. Ice, B. C. Larson, W. Yang, J. Z. Tischler, and J. D. Budai, "The Three-Dimensional X-ray Crystal Microscope: A New Tool for Materials Characterization," Metall Mater Trans A **35,** 1963–1967 (2004).

[79] E. Vlieg, "Integrated Intensities Using a Six-Circle Surface X-ray Diffractometer," J Appl Cryst **30,** 532–543 (1997).

[80] B. C. Larson and L. E. Levine, "Submicrometre-Resolution Polychromatic Three-Dimensional X-ray Microscopy," J Appl Cryst **46,** 153–164 (2013).

[81] J. A. Nelder and R. Mead, "A Simplex Method for Function Minimization," The Computer Journal **7,** 308–313 (1965).

[82] J. Couderc, G. Garigue, L. Lafourcade, and Q. Nguyen, "Standard X-ray Diffraction Powder Patterns," Zeitschrift für Metallkunde **50,** 708–716 (1959).

[83] M. C. M. Rodrigues and M. Militzer, "Application of the Rolling Ball Algorithm to Measure Phase Volume Fraction from Backscattered Electron Images," Materials Characterization **163,** 110273 (2020).

[84] C. K. Chow and T. Kaneko, "Automatic Boundary Detection of the Left Ventricle from Cineangiograms," Computers and Biomedical Research **5,** 388–410 (1972).

[85] J. Sauvola and M. Pietikäinen, "Adaptive Document Image Binarization," Pattern Recognition **33,** 225–236 (2000).

[86] R. C. Gonzalez and R. E. Woods, *Digital Image Processing*, 3rd ed ed. (Prentice Hall, Upper Saddle River, N.J, 2008).

[87] N. Otsu, "A Threshold Selection Method from Gray-Level Histograms," IEEE Transactions on Systems, Man, and Cybernetics **9,** 62–66 (1979).

[88] J. N. Kapur, P. K. Sahoo, and A. K. C. Wong, "A New Method for Gray-Level Picture Thresholding Using the Entropy of the Histogram," Computer Vision, Graphics, and Image Processing **29,** 273–285 (1985).

[89] M. I. Sezan, "A Peak Detection Algorithm and Its Application to Histogram-Based Image Data Reduction," Computer Vision, Graphics, and Image Processing **49,** 36–51 (1990).

[90] Sternberg, "Biomedical Image Processing," Computer **16,** 22–34 (1983).

[91] S. R. Sternberg, "Grayscale Morphology," Computer Vision, Graphics, and Image Processing **35,** 333–355 (1986).

[92] M. Thoma, "The Twiddle Algorithm,", https://martin-thoma.com/twiddle/twiddle/, 2014.

[93] P. Virtanen *et al.*, "SciPy 1.0: Fundamental Algorithms for Scientific Computing in Python," Nat Methods **17,** 261–272 (2020).

[94] G. Swislow, "Spec,", Certified Scientific Software, 1996.

[95] W. Liu, P. Zschack, J. Tischler, G. Ice, and B. Larson, "X-ray Laue Diffraction Microscopy in 3D at the Advanced Photon Source," AIP Conference Proceedings **1365,** 108–111 (2011).

[96] L. Beitra, M. Watari, T. Matsuura, N. Shimamoto, R. Harder, and I. Robinson, "Confocal Microscope Alignment of Nanocrystals for Coherent Diffraction Imaging," AIP Conference Proceedings **1234,** 57–60 (2010).

[97] O. Kovalenko, C. Brandl, L. Klinger, and E. Rabkin, "Self-Healing and Shape Memory Effects in Gold Microparticles through the Defects-Mediated Diffusion," Advanced Science **4,** 1700159 (2017).

[98] B. E. Warren, *X-Ray Diffraction*, *Dover Books on Physics and Chemistry*, facsim. ed ed. (Dover, New York, 1990).

[99] M. M. Nowell, R. A. Witt, and B. W. True, "EBSD Sample Preparation: Techniques, Tips, and Tricks," Microscopy Today **13,** 44–49 (2005).

[100] M. J. Wilkin, Doctor of Philosophy in Materials Science and Engineering, Carnegie-Mellon University, 2022.

[101] V. Favre-Nicolin, S. Leake, and Y. Chushkin, "Free Log-Likelihood as an Unbiased Metric for Coherent Diffraction Imaging," Sci Rep **10,** 2664 (2020).

[102] N. Porter, "Interactive CDI,", Zenodo, 2023.